



HAL
open science

Mechanical Impact of Heterogeneously Distributed H₂O on Quartz Deformation

Petar Pongrac, Petr Jeřábek, Holger Stünitz, Hugues Raimbourg, Martin Racek, Michael C Jollands, Nils Gies, Mona Lueder, Ondrej Lexa, Lucille Nègre

► **To cite this version:**

Petar Pongrac, Petr Jeřábek, Holger Stünitz, Hugues Raimbourg, Martin Racek, et al.. Mechanical Impact of Heterogeneously Distributed H₂O on Quartz Deformation. *Journal of Geophysical Research: Solid Earth*, 2024, 129 (8), 10.1029/2023JB027566 . insu-04883415

HAL Id: insu-04883415

<https://insu.hal.science/insu-04883415v1>

Submitted on 13 Jan 2025

HAL is a multi-disciplinary open access archive for the deposit and dissemination of scientific research documents, whether they are published or not. The documents may come from teaching and research institutions in France or abroad, or from public or private research centers.

L'archive ouverte pluridisciplinaire **HAL**, est destinée au dépôt et à la diffusion de documents scientifiques de niveau recherche, publiés ou non, émanant des établissements d'enseignement et de recherche français ou étrangers, des laboratoires publics ou privés.



Distributed under a Creative Commons Attribution 4.0 International License

Mechanical Impact of Heterogeneously Distributed H₂O on Quartz Deformation



Key Points:

- H₂O initially present inside the quartz grains is transferred into grain boundary region during heating, pressurization, and deformation
- A quantity of added H₂O of >0.2 wt.% causes more variable mechanical behavior of the samples due to enhanced cracking
- Dilatant cracks lead to draining of fluid from grain boundaries and make the dissolution-precipitation processes locally less efficient

Correspondence to:

P. Pongrac,
petar.pongrac@geow.uni-heidelberg.de







Citation:

Pongrac, P., Jeřábek, P., Stünitz, H., Raimbourg, H., Racek, M., Jollands, M. C., et al. (2024). Mechanical impact of heterogeneously distributed H₂O on quartz deformation. *Journal of Geophysical Research: Solid Earth*, 129, e2023JB027566. <https://doi.org/10.1029/2023JB027566>

Received 29 AUG 2023
 Accepted 13 JUL 2024

Author Contributions:

Conceptualization: Petar Pongrac, Petr Jeřábek, Holger Stünitz, Hugues Raimbourg
Data curation: Petar Pongrac, Martin Racek, Michael C. Jollands, Nils Gies, Mona Lueder
Formal analysis: Petar Pongrac, Michael C. Jollands, Nils Gies, Mona Lueder
Funding acquisition: Petr Jeřábek, Holger Stünitz, Hugues Raimbourg
Investigation: Petar Pongrac, Holger Stünitz
Methodology: Petar Pongrac, Petr Jeřábek, Holger Stünitz, Hugues Raimbourg, Michael C. Jollands, Nils Gies, Mona Lueder
Project administration: Petr Jeřábek, Holger Stünitz
Resources: Petr Jeřábek, Holger Stünitz, Hugues Raimbourg, Martin Racek

Petar Pongrac¹ , Petr Jeřábek¹ , Holger Stünitz^{2,3}, Hugues Raimbourg³ , Martin Racek¹, Michael C. Jollands⁴ , Nils Gies⁵ , Mona Lueder⁵, Ondrej Lexa¹ , and Lucille Nègre³

¹Institute of Petrology and Structural Geology, Faculty of Science, Charles University, Prague, Czech Republic,

²Department of Geosciences, Arctic University of Norway, Tromsø, Norway, ³Institute of Earth Sciences, University of Orléans, Orleans Cedex 2, France, ⁴Gemological Institute of America, New York, NY, USA, ⁵Institute of Geological Sciences, University of Bern, Bern, Switzerland

Abstract In order to identify relations between mechanical behavior, deformation mechanisms, microstructural properties, and H₂O distribution, Tana-quartzite samples with added H₂O ranging from 0 to 0.5 wt.% were deformed by axial shortening at constant displacement rates, at 900°C and 1 GPa, reaching up to ~30% bulk strain. Samples with lower quantities of added H₂O (0.1 and 0.2 wt.%) were in average ~30 MPa weaker than the as-is samples with no added H₂O. In contrast, samples with more than 0.2 wt.% added H₂O revealed more variable mechanical behavior, showing either weaker or stronger trend. The weaker samples showed strain localization in their central parts in the vicinity of the thermocouple, that is, the hottest parts of the samples, whereas the stronger samples showed localization in their upper, slightly colder parts. Bulk deformation is accommodated by crystal plasticity and dissolution-precipitation processes. Distribution of H₂O in our samples revealed systematic decrease of H₂O content in the interiors of original grains, caused by increasing strain and H₂O draining into grain boundary regions. With increasing content of added H₂O, the quartz recrystallization gradually changes from subgrain-rotation-dominated to crack-induced nucleation, along with increasing quantity of melt/fluid pockets. The unexpected strain localization in the upper parts of stronger samples most likely results from mode-I-cracking that led to drainage of grain boundaries (GB) due to the crack dilatancy effect, and inhibited dissolution-precipitation in the hottest part of the samples next to the thermocouple. The locus of deformation is then shifted to colder regions where more H₂O is available along GB.

Plain Language Summary The mechanical behavior of rocks is reflected by deformation microstructures, and it is usually dependent on available H₂O in the deformation environment. We tested influence of H₂O in quartzite samples by adding various amounts of H₂O prior to deformation experiments, in the range from 0 to 0.5 wt.%. The results showed that samples with up to 0.2 wt.% of added H₂O are generally weaker than the as-is samples, while with H₂O addition of more than 0.2 wt.% mechanical behavior becomes more erratic. These samples showed either weaker or stronger behavior. While plastic deformation in weaker samples is localized mostly in sample regions with the highest temperature, deformation in stronger samples is unexpectedly localized in colder regions. Quartz grains are found to release initially present H₂O from their interiors into grain boundary regions during deformation. Changes in mechanical properties with increasing content of H₂O are closely related with changes in recrystallization processes. The unexpected localization of deformation in the colder regions results from drainage of GB due to the crack dilatancy effect. In the resulting dried GB, the dissolution-precipitation processes would be impeded, while the locus of deformation is shifted to colder parts with more H₂O along the GB.

1. Introduction

Deformation experiments on both synthetic and natural samples have demonstrated that H₂O has a pronounced mechanical weakening effect during crystal plastic deformation of quartz (e.g., Blacic, 1975; Doukhan, 1995; Griggs, 1967, 1974; Hirth & Tullis, 1992; Kohlstedt et al., 1995; Kronenberg & Tullis, 1984; Luan & Pater-son, 1992; McLaren et al., 1989; Palazzin et al., 2018; Pongrac et al., 2022; Post & Tullis, 1998; Rutter & Brodie, 2004; Stipp et al., 2006). Diffusion of external H₂O into the quartz structure is nearly impossible at laboratory time scales (Gerretsen et al., 1989; Kronenberg et al., 1986; Rovetta et al., 1986), so that molecular H₂O is either incorporated into crystals during growth (Rutter & Brodie, 2004) or infiltrated through cracks or microcracks, and eventually captured in the form of fluid inclusions upon crack healing (Fitz Gerald et al., 1991;

© 2024. The Author(s).

This is an open access article under the terms of the [Creative Commons Attribution License](https://creativecommons.org/licenses/by/4.0/), which permits use, distribution and reproduction in any medium, provided the original work is properly cited.

Software: Petar Pongrac, Petr Jeřábek, Michael C. Jollands, Nils Gies, Mona Lueder, Ondrej Lexa
Supervision: Petr Jeřábek, Holger Stünitz, Hugues Raimbourg
Validation: Petar Pongrac, Petr Jeřábek, Holger Stünitz, Hugues Raimbourg, Martin Racek, Michael C. Jollands, Ondrej Lexa, Lucille Nègre
Visualization: Petar Pongrac
Writing – original draft: Petar Pongrac, Holger Stünitz
Writing – review & editing: Petr Jeřábek, Holger Stünitz, Hugues Raimbourg, Martin Racek, Nils Gies

Gerretsen et al., 1989; Kronenberg et al., 1986; Tarantola et al., 2010, 2012). Thus, H₂O is either present originally inside the quartz crystals (e.g., in milky quartz or synthetic “wet” quartz) or, if added, it has to enter the crystals and/or become re-distributed by cracking and crack healing (e.g., Jaoul et al., 1984; Kronenberg et al., 1986; Palazzin et al., 2018; Schmocker et al., 2003; Stünitz et al., 2017).

Adding more H₂O to the deforming quartz samples typically results in a weaker behavior (e.g., Hirth & Tullis, 1992; Kronenberg & Tullis, 1984). However, the added amounts of H₂O in experiments are very small, usually between 0.1 and 0.5 wt.% (e.g., Hirth & Tullis, 1992; Kronenberg & Tullis, 1984). The reason for adding only small amounts of H₂O is that, in order to maintain crystal plastic deformation, pore fluid pressure effects should be avoided. At high pore fluid pressures, the effective confining pressure is reduced, so that the material is expected to undergo brittle deformation (e.g., Beeler et al., 2016). When crystal plastic deformation at elevated temperatures takes place, fluid filled pores become isolated and the fluid pressure inside the pores will be close or equal to the lithostatic confining pressure ($P_{\text{fluid}} \approx P_{\text{lithostatic}}$). Conventionally, such conditions are considered to be mechanically unstable (e.g., King Hubbert & Rubey, 1959; Terzaghi, 1943). However, virtually all petrological treatments of fluids in metamorphic rocks require the $P_{\text{fluid}} = P_{\text{total}}$ condition. One simple way out of this apparent contradiction is that at very small volume fractions of pores in the rock (the typical situation in metamorphic rocks), the mechanical effect of the pore pressure becomes less important, so that most metamorphic rocks show sufficient mechanical strength. A possible treatment of this situation can be the concept of effective pressure coefficient (Hirth & Beeler, 2015; Terzaghi, 1943). Recently, pore fluid pressure studies attempted to give physical explanations to rationalize the effective pressure coefficient (Beeler et al., 2016; Hirth & Beeler, 2015; Scholz & Cowie, 1990). Another approach to the solution is to investigate the aspect of volume proportions of added fluid in experiments (e.g., French et al., 2019; Kronenberg & Tullis, 1984). In this study, we are following the latter course, trying to obtain data and observations on mechanical effects of small amounts of H₂O added (0–0.5 wt.%) to simulate conditions at elevated pressures and temperatures at or slightly above fluid saturation. The well-known mechanical weakening effect of the H₂O for crystal plastic deformation in quartz is studied in conjunction with potential pore pressure effects (brittle deformation) in order to give new insight in the complexity of the mechanisms and processes taking place at small scale during the brittle-viscous transition.

2. Experiments and Analytical Methods

The experimental material used in this study is a late Precambrian quartzite from the Tana region (ELKEM quarry, Austertana) in northern Norway. A detailed characterization of this material is given by Nègre et al. (2021) and Pongrac et al. (2022). The grain size is ~200 μm and the concentration of impurities (phyllosilicates, Fe oxides + hydroxides) is estimated to be ≤1 vol.% (Pevik, 2015).

2.1. Sample Preparation and Deformation Experiments

All deformation experiments were carried out in the deformation laboratory at the Department of Geosciences in Tromsø, Norway, in an axial shortening set-up using the Griggs-type solid medium apparatus (Griggs, 1967; T. E. Tullis & Tullis, 1986) at confining pressure of 1 GPa, temperature of 900°C and constant displacement rates resulting in strain rates of $\sim 1.5 \times 10^{-6} \text{ s}^{-1}$.

The applied force was measured using an external load cell. The displacement of σ_1 piston was recorded by a Linear Variable Differential Transformer with a resolution of ~1 μm. The differential stress was calculated as $\Delta\sigma = \sigma_1 - \sigma_3$ ($\sigma_2 = \sigma_3$) with the minimum and the maximum principal stresses calibrated with respect to the confining pressure at the hit-point (see Appendix 2 in Pongrac et al., 2022). The error in the differential stress determination is controlled by the external load cell sensitivity. Even though the error may vary with respect to the stress level, for the stress range obtained in this study, we assume that it lies in the typical range of ±30 MPa given by Holyoke and Kronenberg (2010) for a solid medium apparatus. A more precise error estimate cannot be given at this stage. A more detailed explanation of the data evaluation process and application of the corrections is available in Pec (2014) and Pongrac et al. (2022).

Cylindrical cores with diameters of 6.35–6.55 mm and lengths of 13–14 mm were ground parallel and normal to the cylinder axis. All sample cores were pre-dried at ~115°C for approximately 24 hr, wrapped in Ni foil and inserted into pre-annealed Pt-jackets. In addition to the as-is and 0.1 wt.% H₂O-added samples studied in Pongrac et al. (2022), samples with 0.2, 0.3, 0.4, and 0.5 wt.% of added H₂O were investigated in this study. After the sample encapsulation, Pt-jackets were weld-sealed.

In the sample assembly, alumina pistons with a diameter of ~ 6.33 mm were used as pressing pistons, and solid NaCl was used as a confining medium. For temperature control, S-type thermocouples were used, placed at $\sim 30\%$ of the initial sample length. The temperature between the measuring point and the bottom of the upper alumina forcing piston is estimated to be up to 10% lower (Pec et al., 2016). For more detailed description of the sample assembly and experimental procedures, see Appendix 1 in Pongrac et al. (2022).

2.2. Fourier-Transform Infrared Spectroscopy

Thick sections used for the Fourier-transform infrared spectroscopy (FTIR) were prepared at the Institute of Earth Sciences, University of Orleans, where the FTIR measurements were carried out. The thick sections were polished and their thicknesses measured optically (typically ~ 100 μm). IR spectrometry measurements were performed using a Nicolet-6700 (ThermoFisher Scientific) spectrometer with Nicolet Continuum infrared microscope. The spectrometer was purged with dry air to reduce air moisture and all spectra were measured at room temperature. The spectrometer is equipped with a liquid nitrogen cooled MCT detector and XT-KBr beam-splitter. Wave-number range of the obtained spectra was between 1,500 and 5,500 cm^{-1} , using non-polarized light. The window aperture for the measurements covered a squared area of 20×20 to 40×40 μm , and a $32\times$ infinity corrected Schwarzschild objective (matching to $32\times$ condenser) was used. A background spectrum of the air and a transparent calcium fluoride sample bearing window was collected every 1–2 hr and subtracted from the subsequent sample spectra. The H_2O content was measured in different parts of each sample with 64 or 128 scans per spectrum (depending on the spectrum quality) and resolution of 4 cm^{-1} . A more detailed description of the H_2O content measuring and determination, as well as the data treatment is available in Appendix A.

For the processing of the FTIR focal plane array (FPA) maps the atmospheric correction and concave rubber band correction with 64 points and 4 iterations were carried out using OPUS® (version 8.5). The spectra were then exported and further processed with the in-house developed MATLAB software SpecXY (available on request). The spectra were normalized to 1 cm thickness and integrated absorbance for different maps were generated, by extracting the chosen part of the signal, performing a linear baseline correction between the integration endpoints, and integrating the corrected spectra.

2.3. Microstructure and Texture Analysis

Thin sections of deformed samples were prepared and analyzed at the Institute of Petrology and Structural Geology, Charles University in Prague by means of (a) light microscopy in cross-polarized light, (b) cathodoluminescence (CL) imaging, (c) electron microprobe (EMPA), (d) scanning electron microscope (SEM), and (e) electron backscatter diffraction (EBSD).

Thermionic CL and element maps were obtained using the FEG EPMA JEOL JXA-8530F equipped with the integrated cathodoluminescence spectrometry system xCLent IV, with acceleration voltage of 15 kV, probe current of 40–50 nA and a step size between 0.25 and 1.5 μm . EPMA was also used for backscatter electron (BSE) imaging. Non-thermionic (“cold”) CL images were obtained at the Czech Geological Survey in Prague, using the CITL Mk5–2 CL microscope, at 700 mA with a capture time of 3–6 s.

EBSD results were acquired in point-beam mode at 20 kV and 7 nA using the Tescan Vega SEM, equipped with NordLys Nano detector (Oxford Instruments). The EBSD data were collected using the AZtec software (Oxford Instruments) and processed using Matlab toolbox MTEX 4.5.1 (Hielscher & Schaeben, 2008). In the EBSD maps, the grains were reconstructed using the grain segmentation method of Bachmann et al. (2011). In order to avoid pseudo-symmetric boundaries (60° rotation around (0001)), the trigonal symmetry-3m (321 group) of the EBSD data set was changed to the hexagonal symmetry (622 group). Threshold of three neighboring pixels with misorientation $< 2^\circ$ was used to distinguish grain/subgrain boundary in the EBSD grain maps. Grains are separated by high angle grain boundaries defined by misorientation angle $> 10^\circ$, and subgrains by low angle subgrain boundaries defined by misorientations between 2° and 10° . Crystallographic orientations are colored using the inverse pole figure color coding based on the 622 symmetry and related to direction perpendicular to principal stress σ_1 in the sample section.

Digitized thin section maps of recrystallization domains and original sand grains were constructed using the QGIS open source software and processed using MATLAB toolbox polyLX (Lexa, 2003b). The quantitative microstructural analysis and the strain analysis of digitized original grains was performed by the Python polyLX

Table 1
Experimental Conditions for All Constant Conditions Experiments, at 1 GPa and 900°C

Sample	H ₂ O addition (wt.%)	Flow stress at ~10% strain (MPa)	Peak stress (MPa)	Finite strain (%)	Strain rate (s ⁻¹)	Deformation time (hrs)
547PP	0	179	181	32.02	1.19–1.82 × 10 ⁻⁶	72.8
568PP	0	212	212	31.6	1.25–1.96 × 10 ⁻⁶	69.3
574PP	0	224	225	31.62	1.20–2.04 × 10 ⁻⁶	70.6
541HS	0.1	185	185	31.65	1.20–1.83 × 10 ⁻⁶	71.3
567PP	0.1	183	196	29.75	1.06–1.59 × 10 ⁻⁶	75.9
576PP	0.1	156	157	31.37	1.23–1.89 × 10 ⁻⁶	69.7
543PP	0.2	189	197	32.08	1.27–1.94 × 10 ⁻⁶	69.4
566PP	0.2	161	166	32.03	1.24–1.91 × 10 ⁻⁶	71.3
586PP	0.2	185	230	31.42	1.20–1.95 × 10 ⁻⁶	70.9
564PP	0.3	121	125	31.29	1.21–1.79 × 10 ⁻⁶	71.1
588PP	0.3	245	271	26.34	1.19–1.59 × 10 ⁻⁶	61.1
565PP	0.4	295	301	32.23	9.08 × 10 ⁻⁷ – 1.88 × 10 ⁻⁶	92.8
591PP	0.4	182	185	32.80	1.20–1.79 × 10 ⁻⁶	74.5
545PP	0.5	208	224	32.49	1.24–1.91 × 10 ⁻⁶	72.2
569PP	0.5	172	187	30.71	1.23–1.85 × 10 ⁻⁶	67.9
597PP	0.5	232	258	28.06	1.18–1.84 × 10 ⁻⁶	64.3

Note. Results of as-is and 0.1 wt.% H₂O-added experiments were presented in Pongrac et al. (2022). Due to continuous decrease in sample length during the experiment, both the initial and the final strain rates are listed.

package (<https://github.com/ondrolexa/polylyx>; Lexa, 2023) using the surface projection (SURFOR) functions (Heilbronner & Barrett, 2014; Panozzo, 1983). Strain across the samples was determined by a moving window, with dimensions 1/6 of vertical direction and width of the analyzed strip. Strain is calculated as the ratio between maximum and minimum of the SURFOR functions of individual grains within the moving window.

3. Results

3.1. Mechanical Behavior of Quartz With Increased H₂O Content

Details on experimental conditions of all experiments with different amounts of added H₂O are listed in Table 1, and mechanical data presented as differential stress versus strain curves are shown in Figure 1. It is important to note that, even though the displacement rates were constant, there is a small increase in strain rates due to decreasing sample length.

The stress versus strain curves for samples with low quantities of added H₂O (low-H₂O samples; up to 0.2 wt.%) show steady state flow stresses in the range of ~150–225 MPa (Figure 1a). The flow stress values for all samples in Table 1 are defined as the stresses at ~10% strain (between 10% and 15% strain most stress-strain curves are horizontal). The average flow stresses (at ~10%) strain are ~30 MPa lower for 0.1 and 0.2 wt.% H₂O-added samples compared to the as-is ones (Figure 1b). While for the 0.1 wt.% H₂O-added samples this difference is systematic until 30% strain, most 0.2 wt.% H₂O-added samples behave in a similar way, but one sample reaches similar values as the average of the as-is samples at 30% strain (Figure 1b). The low-H₂O samples show minor weakening after ~20–25% strain, with the exception of 0.2 wt.% H₂O-added sample 586PP.

Samples with higher quantities of added H₂O (high-H₂O samples; 0.3–0.5 wt.%) show a more erratic mechanical behavior and steady state flow stresses spreading between ~120 and ~300 MPa (Figure 1c). The erratic behavior is manifested by distinct variations in the stress versus strain curves for samples with the same quantity of added H₂O showing either stronger or weaker behavior compared to the low-H₂O samples. The weaker samples (564PP, 569PP, 591PP, 545PP) show steady state flow stresses comparable with the low-H₂O samples (cf. gray area in Figures 1a and 1c). In contrast, the stronger samples show higher stresses and strain hardening (597PP, 588PP). The strongest sample 565PP shows steady state flow at ~300 MPa, followed by strain weakening between 23%

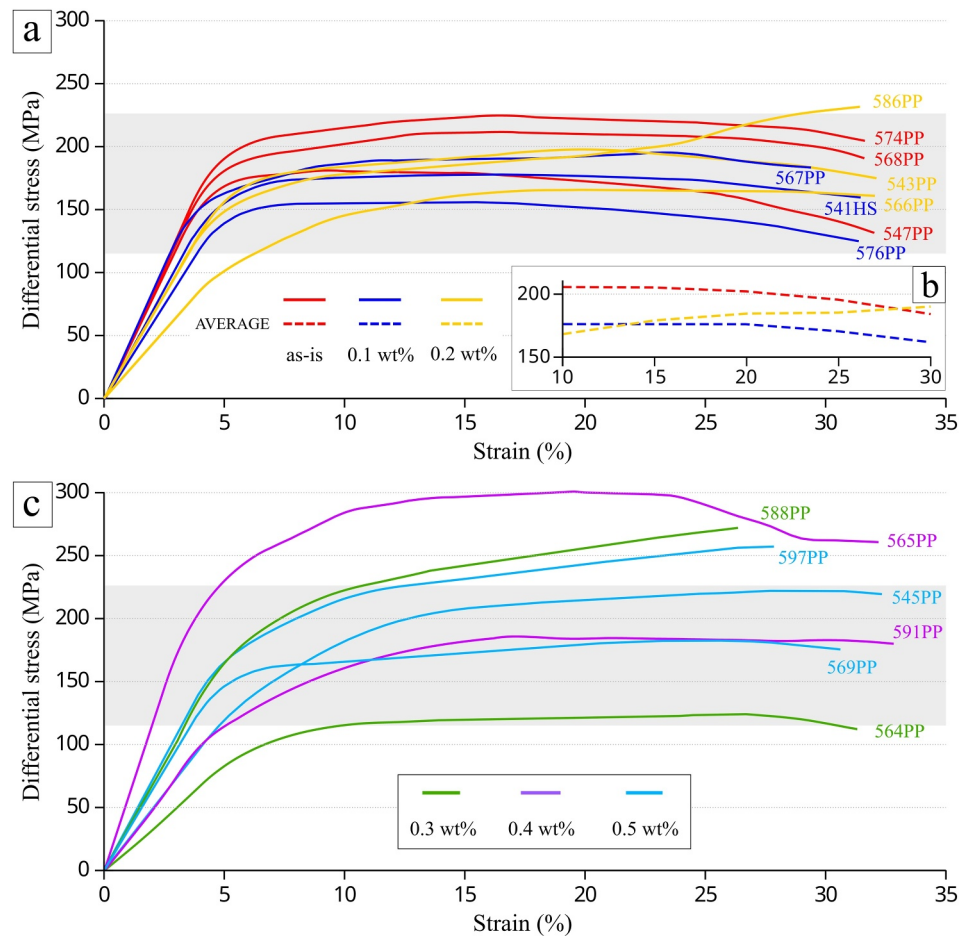


Figure 1. Differential stress versus strain curves for axial shortening experiments with (a) low (0–0.2 wt.%) and (c) high (0.3–0.5 wt.%) contents of added H₂O. (b) Curves showing arithmetic mean of differential stresses calculated for samples with the same H₂O addition, for the range from 10% to 30% strain. The gray shaded region covers the stress range of the weaker samples for both low and high contents of added H₂O (a, b). All experiments were carried out at 1 GPa, 900°C and constant displacement rates (strain rates are listed in Table 1).

and 29% strain with subsequent steady state flow at ~260 MPa. For the purpose of further description, we distinguish two groups of samples: (a) the weaker samples with flow stresses of 125–225 MPa (gray shaded region in Figure 1) and (b) the stronger samples with flow stresses of 225–300 MPa. The weaker samples represent the majority of our experiments while only three samples belong to the stronger group.

3.2. Strain Localization in the Weaker and Stronger Samples

The weaker samples are characterized by more homogeneously shortened barrel-like shapes after the deformation, with bulged out (more shortened and widened) regions occurring in the vicinity of the thermocouple position (Figure 2a). On the contrary, the stronger samples show more irregular shapes, with bulged out regions being localized in the upper part of the samples, where the temperature is estimated to be up to 10% lower than the temperature at the thermocouple position (Pec et al., 2016; see their methods section).

This relationship can be presented statistically by the angle α defined as the angle between (a) the line connecting the most barreled point (in 2D) at the sample edge in the vertical section and the farthest corner of the sample at the same edge (sample edge line; red lines in Figure 2b), and (b) direction of principal stress σ_1 . Visual inspection of deformed samples indicates that samples are barreled in a symmetric way, so that the 2D sections represent the rotational symmetry. The sample edge (red line in Figure 2b) was obtained after a statistical linear regression of all the points of the sample edge from its upper end to the most barreled part. As the edges of some samples are quite irregular, the most outward bulged points were determined using a simplified edge (dashed green line in

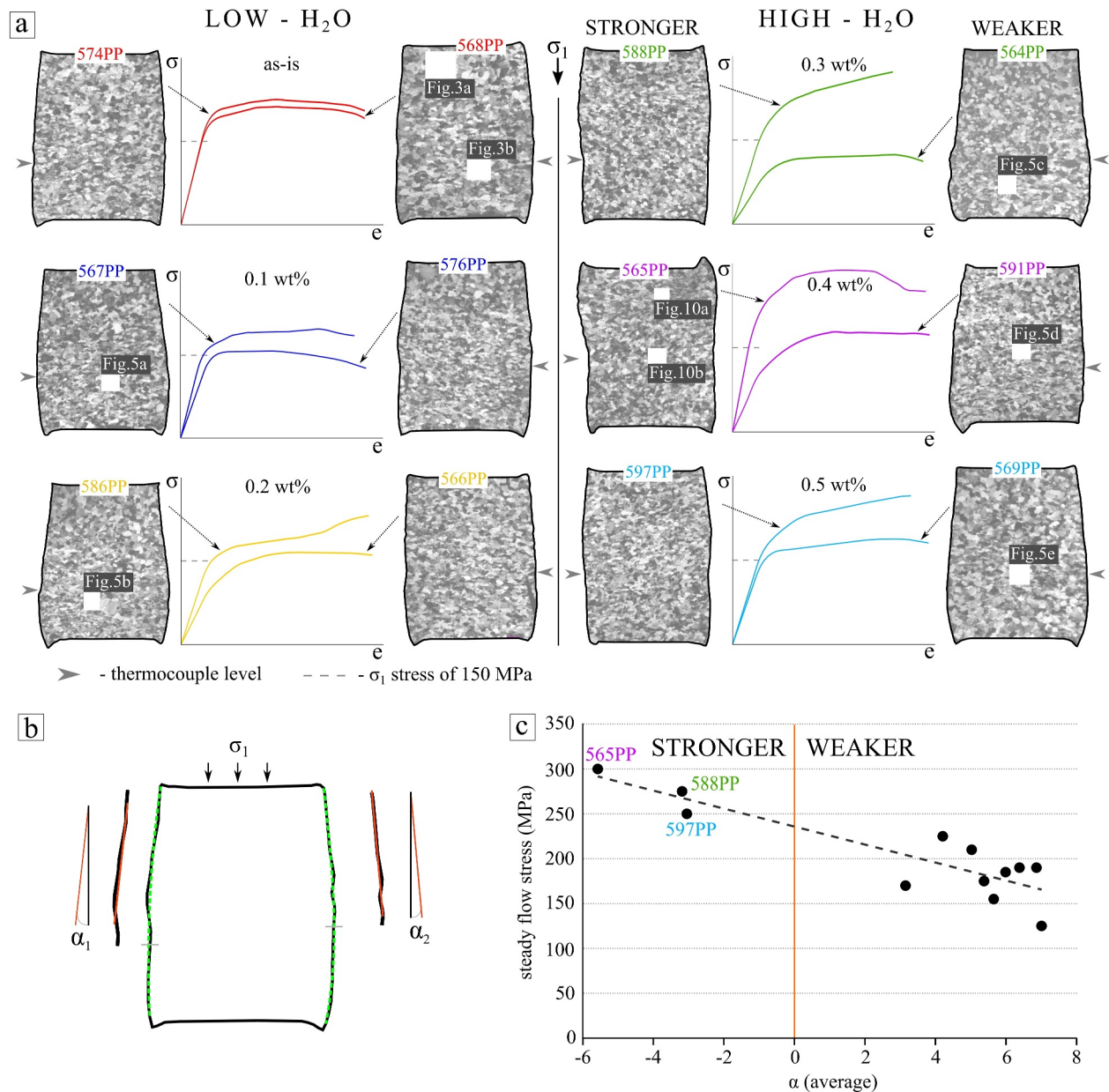


Figure 2. (a) Differences in the shape of samples after deformation experiments related to their flow stress. Scans of sample thin sections are in cross-polarized light. White rectangles mark positions of microstructure images shown in other associated figures. (b) Example of the determination of the angle α between the sample edge line (red) and the direction of principal stress σ_1 . The horizontal gray dashes on the sample edge mark the most bulged points on the simplified sample edge (dashed green line). (c) Relationship between the average of the left and right α -angles (α_1 and α_2) as explained in (b) and the differential stresses at the steady state of deformation (at $\sim 15\%$ strain).

Figure 2b). The larger α thus corresponds to more homogeneous barrel-like shape of the samples bulged out in the vicinity of the thermocouple (the highest temperature), while negative α values correspond to sample shapes bulged out at the upper parts, farther from the thermocouple (e.g., samples 565PP, 588PP, and 597PP in Figure 2a). The angle α is determined for all thin sections presented in Figure 2a, and systematic relationship between the steady flow stress and the α -angles is shown in Figure 2c. The correlation between the α and stresses at $\sim 15\%$ strain (where mechanical behavior is closest to steady state flow) shows that higher stresses are associated with negative α -angles. It is important to note that presented irregular finite shapes of the deformed samples result in relatively small variations of local strain rates across the samples (assuming deformation during the whole duration of the experiment).

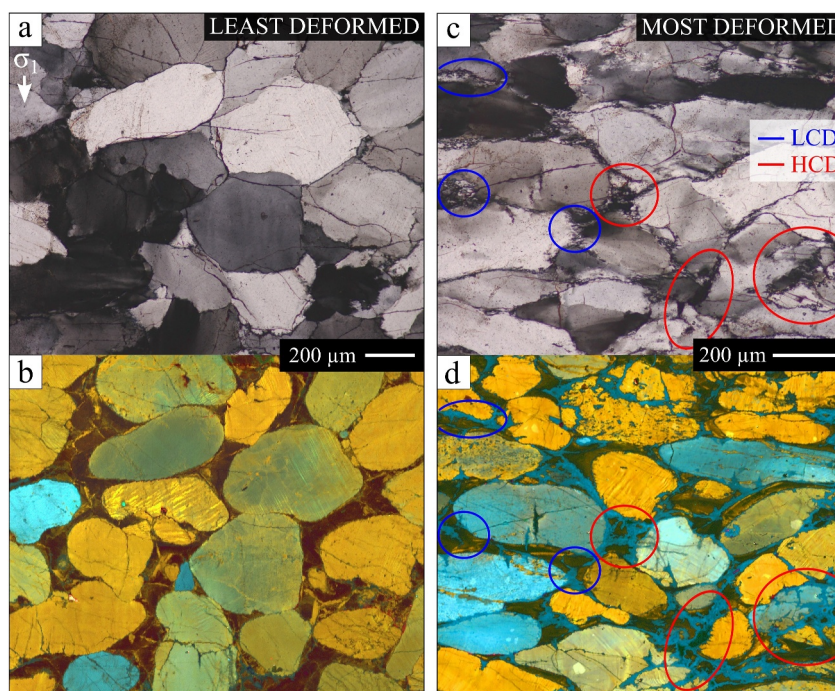


Figure 3. Comparison of the microstructures of (a, b) the least and (c, d) the most deformed parts of samples after deformation, on the example of the as-is sample 568PP. Images (a) and (c) show microstructures in cross-polarized light, and (b) and (d) in cathodoluminescence. Blue and red circles/ellipses mark examples of low (low crack density) and high (high crack density) crack density domains, respectively.

3.3. Microstructures of the Weaker Samples

The weaker samples, characterized by regular barrel-like shapes after the deformation (positive α -angles; Figure 2), are nearly undeformed in their upper part and show intense deformation near the level of the thermocouple position. The least deformed regions (Figures 3a and 3b) show only minor signs of deformation and a microstructure comparable to that of the starting material (for the micrographs and details on the starting material see Figure 3 in Pongrac et al., 2022). Cathodoluminescence (CL) images of these regions document that the grains of the starting material consist of rounded sand grains in the original sediment (combinations of yellow, orange and cyan-blue) and SiO₂ overgrowths (cement; dark brown) that fill the former pore space between the sand grains. Overgrowths and sand grains are in crystallographic continuity (cf. Figures 3a and 3b). The original undeformed quartz grains show neither shape nor crystal preferred orientation and their average grain size is $\sim 200 \mu\text{m}$ (Negre et al., 2021).

The most deformed parts of the samples show undulatory extinction and flattening of the original quartz grains accompanied by recrystallization and cracking (Figures 3c and 3d). The zones of cracking and recrystallization are associated with the appearance of a prominent blue luminescence (Figures 3c and 3d).

In this study, the term “recrystallization” is used for all processes that result in formation of new smaller grains from initially bigger grains, including the cracking-induced recrystallization (see below). In our previous work, carried out using the same as-is and 0.1 wt.% H₂O-added samples (Pongrac et al., 2022), two types of recrystallized domains had been distinguished on the basis of the relative density of cracks. These are the low crack density (LCD) and the high crack density (HCD) recrystallized domains (blue and red ellipses in Figures 3c, 3d, and 4). In addition to the crack density (Figure 4c), the two domains are distinguished by several additional microstructural criteria. The LCD domains usually occur along an inclined interface between two original grains, and the HCD domains occur mostly at the triple junctions of the original grains. Recrystallized grains in the HCD domains show rounded to angular shapes with larger and more heterogeneous grain size (Figure 4d). In contrast, recrystallized grains in the LCD domains rarely exceed $\sim 7 \mu\text{m}$ in diameter and show slightly elongated shapes with the long axis perpendicular to the principal stress σ_1 . The HCD recrystallized domains are associated with

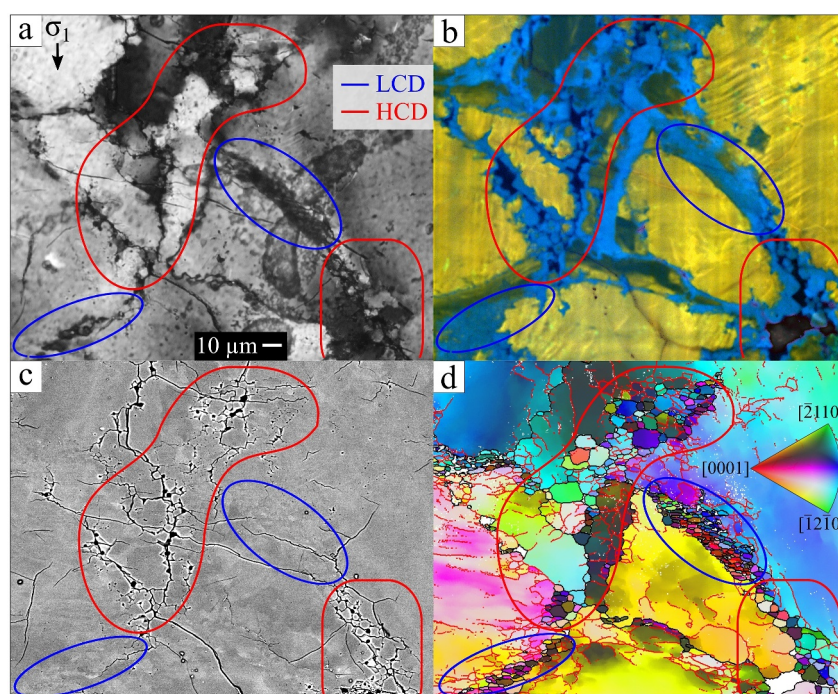


Figure 4. Comparison of the low crack density and high crack density domains in the most deformed part of the sample 567PP, marked by blue and red ellipses, respectively. The representative area is shown in (a) cross-polarized light, (b) cathodoluminescence map, (c) backscatter electron image and (d) electron backscatter diffraction (EBSD) map. The EBSD map shows individual quartz grains with crystallographic orientation colored by the inset inverse pole figure scheme related to direction perpendicular to principal stress σ_1 in the sample section; high angle grain boundaries are marked by black, and low angle subgrain boundaries by red.

pockets and channels filled by amorphous material (identified as quenched melt; Pongrac et al., 2022) with no luminescence (see red regions in Figure 4b and CL insets in Figures 5a and 5b).

In the LCD recrystallized domains, some portions of recrystallized grains do not show change in luminescence but preserve their original brown (cement-related) or yellow (sand grain-related) luminescence (e.g., green arrows in Figure 5a). The angular grains in the HCD recrystallized domains locally show the original luminescence in their cores and blue luminescent overgrowth rims, sometimes with idiomorphic shapes (e.g., orange arrows in Figure 5b). Such idiomorphic grains always occur in association with amorphous pockets and channels in the HCD recrystallized domains (highlighted by white polygons in the CL maps in Figure 5).

As documented by Pongrac et al. (2022), the crystallographic orientation relations between porphyroclasts and recrystallized grains indicate recrystallization by subgrain rotation in the LCD domains and by growth of cracked fragments in the HCD domains. This is also consistent with the microstructural criteria described above. However, recrystallization of both LCD and HCD domains was accompanied by grain boundary migration leading to reconstitution of quartz and associated change in luminescence to blue, making the distinction between the two recrystallization mechanisms difficult in certain places.

3.3.1. Changes in Microstructure With Increased H₂O Content

The representative microstructures in the most deformed parts of the weaker samples (positive α -angles; Figure 2) with different quantities of added H₂O are presented in cross-polarized light and CL in Figure 5, showing the differences related to the increasing H₂O content. The low-H₂O samples show a similar proportion of LCD and HCD recrystallized domains, while the HCD domains and the amorphous pockets (quenched melt) with idiomorphic new grains associated with HCD domains become more dominant in the high-H₂O samples (cf. Figure 5a–5e). The area fraction of amorphous pockets in the most deformed parts of the weaker samples (marked by white in CL images in Figure 5) increases gradually from 0.95% in the 0.1 wt.% H₂O-added sample to 4.03% in the 0.5 wt.% H₂O-added sample. In the 0.5 wt.% H₂O-added samples, local networks of melt channels and pockets

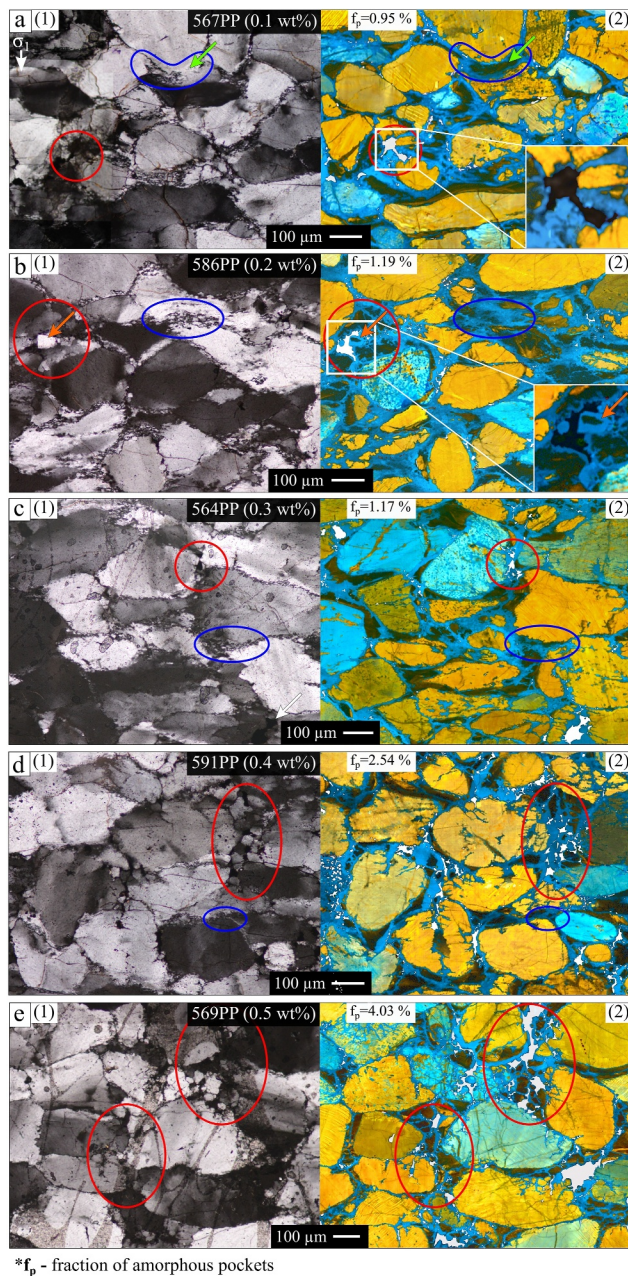


Figure 5. Microstructures in the most deformed parts of the weaker samples (see text for explanation) with changing quantity of added H₂O: (a) 0.1 wt.% H₂O-added sample 567PP, (b) 0.2 wt.% H₂O-added sample 586PP, (c) 0.3 wt.% H₂O-added sample 564PP, (d) 0.4 wt.% H₂O-added sample 591PP and (e) 0.5 wt.% H₂O-added sample 569PP; in (1) cross-polarized light and (2) cathodoluminescence (CL). Blue and red ellipses mark examples of low crack density (LCD) and high crack density (HCD) recrystallized domains, respectively. White polygons in the CL images mark pockets and their networks, with stated volume fraction (f_p). The insets in (a) and (b) zoom to the amorphous pockets. Green arrows in (a) show an example of clusters of LCD-recrystallized grains that preserve the original luminescence; orange arrows in (b) show an example of cracked fragments associated with amorphous pockets.

can be seen, with size of the pockets of up to 100 μm (Figure 5e). Overall, the 0.4 and 0.5 wt.% H₂O-added samples are more intensely cracked and show less pronounced grain flattening compared to the low-H₂O samples. In addition, the cracked fragments are generally larger with increasing H₂O content (see HCD domains in Figures 5a–5e).

Extent and orientation of recrystallized material was quantified from digitized (polygonized) LCD and HCD domains for increasing content of H₂O (Figure B1). The total proportion of recrystallized material in the digitized maps from the most deformed parts of the weaker samples ranges between 19% and 26%, with no systematic relation to the quantity of added H₂O. However, with increasing content of added H₂O from 0 (as-is sample) to 0.5 wt.%, the proportion of LCD recrystallized domains gradually decreases from 15.3% to 2%, while the proportion of HCD domains increases from 7.3% to 21.4% (Figures B1 and 6). This relationship is demonstrated by the change in the area fraction of LCD and HCD recrystallized domains calculated as $A_{\text{LCD}}/A_{\text{HCD}}$ (Figure 6). The $A_{\text{LCD}}/A_{\text{HCD}}$ gradually decreases from 2.09 for the as-is sample, to 0.09 for the 0.5 wt.% H₂O-added sample. The LCD domains show more complex, elongated and lobate shapes, while the HCD domains show more rounded (convex) equi-dimensional shapes (Figure B1). The rose diagrams in Figure B1 show strong shape preferred orientation of LCD domains perpendicular or sub-perpendicular to the shortening direction. In contrast, the HCD domains in general show only weak shape preferred orientation parallel to the shortening direction.

3.3.2. Quenched Melt Pockets in Low- and High-H₂O Samples

The BSE images show that the above-described pockets are not always filled with detectable amorphous matter (present as quenched melt and characterized by a higher BSE contrast; Pongrac et al., 2022). In case of filled pockets, the quenched melt contains spherical pores and sporadically crystallized Al-Si phases (Figure 7a). In the case of unfilled (empty) pockets, the detectable amorphous matter is sparsely present in the form of pocket rims or smaller clusters (Figure 7b). In the as-is samples, the majority of the pockets are filled, while with increasing H₂O, they are mostly unfilled. In the 0.5 wt.% H₂O-added sample, pockets with detectable amorphous matter are rarely found.

The chemical composition of the amorphous matter in the pockets was determined by EDS (energy-dispersive spectroscopy), from 10 measuring points in each sample covering the entire H₂O-addition range. List of the major constituents and their proportions, together with technical details on the EDS evaluation, is presented in Appendix C. The average content of SiO₂, Al₂O₃, and H₂O is similar for all the analyzed samples with 69.8 wt.% \pm 1.7 of SiO₂, 11.7 wt.% \pm 1 of Al₂O₃ and 11.6 wt.% \pm 1.2 of H₂O. The content of other major constituents shows compositional differences between the low- and high-H₂O samples manifested by comparatively lower K₂O and FeO and higher Na₂O in the high-H₂O samples (Figure D1a). Other elements, which appear in much lower proportions, are presented as atomic ratio in Figure D1b, showing a general increasing trend of Cl-content, and decrease in content of Mg, P, and Ca with addition of H₂O. Figure D1c shows decrease in content of K, Ca, Mg, and Fe with increase in content of Na.

3.4. H₂O Quantification and Distribution

The H₂O content was analyzed by FTIR in 11 samples, measuring 2 samples of each quantity of added H₂O, except for the 0.4 wt.%, where only one

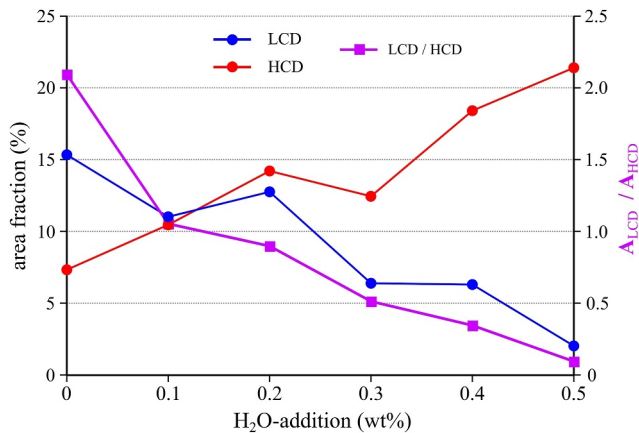


Figure 6. Total area fraction of low crack density (LCD) (blue) and high crack density (HCD) (red) digitized recrystallized domains (see Figure B1) as a function of quantity of added H₂O. The purple line presents changes in ratio of LCD and HCD area fraction (A_{LCD}/A_{HCD}).

sample was measured (591PP). The FTIR measurements in each sample covered (a) original grains in the least deformed part, (b) deformed original grains in the most deformed part, and (c) boundary regions between the original grains in the most deformed part. For the grain interior measurements, a larger window aperture of $40 \times 40 \mu\text{m}$ was used. For the grain boundary region measurements, the smallest possible aperture of $20 \times 20 \mu\text{m}$ was used in order to reduce the effect of adjacent areas. Some spectra for the grain boundary regions were obtained using extended window aperture of $40 \mu\text{m} \times 20 \mu\text{m}$, aligned with GB. It is important to note that small cracks and GB of adjacent recrystallized domains had probably been included in some of the grain boundary region measurements. However, visible cracks, and quenched melt pockets were avoided during measurements. The list of the FTIR-analyzed samples with corresponding analytical details is presented in Appendix E. The positions of absorption bands observed in our spectra (for defined wavenumber ranges of the Al- and mica-related OH discrete bands see the text of Appendix A) are in excellent agreement with positions reported in the literature (e.g., Aines & Rossman, 1984; Gleason & DeSisto, 2008; Jollands et al., 2020; Kats, 1962; Kronenberg, 1994; Kronenberg et al., 1986; Niimi et al., 1999; Stünitz et al., 2017).

Quantification of discrete OH-bands show that the highest average absorbance for Al- and mica-related OH⁻ were obtained from the grain boundary region, while their lowest concentrations were obtained from interiors of the most deformed grains (Figure F1). Most of the OH in samples is present in the form of molecular H₂O. The amount of H₂O in individual measurements was determined using the integrated absorbance (area under the molecular H₂O absorption broadband; Appendix A) and the Beer-Lambert law, following Aines et al. (1984), Stalder (2021), and Libowitzky and Rossman (1997) (see the Methods section for detailed explanation). The contents and distribution of H₂O in Figure 8 present individual measurements from all analyzed samples for each amount of H₂O-addition and the above-defined measurement category. In the least deformed grains, frequency of H₂O concentrations shows somewhat unsystematic distributions, with quite large overall spread (most of the measurements in the range from 0 to 5,000 H/10⁶ Si). In contrast, in the most deformed grains more than 70% of the measurements in all samples showed H₂O concentrations lower than 1,000 H/10⁶ Si. In the grain boundary regions, H₂O concentrations show higher frequency of lower values in the low-H₂O samples whereas with increasing added H₂O the distribution of H₂O concentrations becomes more scattered with a pronounced frequency shift toward higher values (right side of the histogram).

The average H₂O concentrations in individual samples (usually two per each H₂O-addition) are presented in Figure 9. The least deformed grains in all samples show a wide range of H/10⁶ Si molar concentrations, with an average near 2,700 H/10⁶ Si (blue dashed line in Figure 9) and no systematic trend with respect to the quantity of added H₂O. The most deformed grains contain systematically lower concentrations, in a narrower range around 1,200 H/10⁶ Si (red dashed line in Figure 9), regardless of the H₂O-addition. Considerably lower concentrations in the more deformed grains imply a release of the initially present H₂O from the quartz grains during deformation. The difference between average H₂O concentrations in all least deformed and most deformed grains (blue and red dashed line, respectively, in Figure 9) shows an average H/10⁶ Si loss of ~1,500 (equivalent to ~0.02 wt.%). This value corresponds approximately to the H₂O-content of the grain boundary regions of as-is samples (Figure 9). The average H₂O concentration in the grain boundary regions shows a general trend of increase from ~1,300 H/10⁶ Si in the as-is samples to ~3,300 H/10⁶ Si in the 0.5 wt.% samples (Figure 9).

3.5. Microstructures of the Stronger Samples

Contrary to the group of the weaker samples with the barrel-like shapes and bulged out parts at the level of thermocouple (i.e., positive α -angles; Figure 2), the stronger samples show rather irregular shapes, with the bulged out parts occurring in the upper regions of the samples (i.e., negative α -angles; Figure 2). Such geometry is unexpected due to lower temperatures in the upper regions of the samples with respect to the thermocouple level (Pec et al., 2016; see the methods section for more details). In the upper regions, the stronger samples contain flattened original grains with a high degree of undulatory extinction and dense networks of relatively short and narrow cracks, while regions in the vicinity of the thermocouple show only extensive cracking, exposing longer

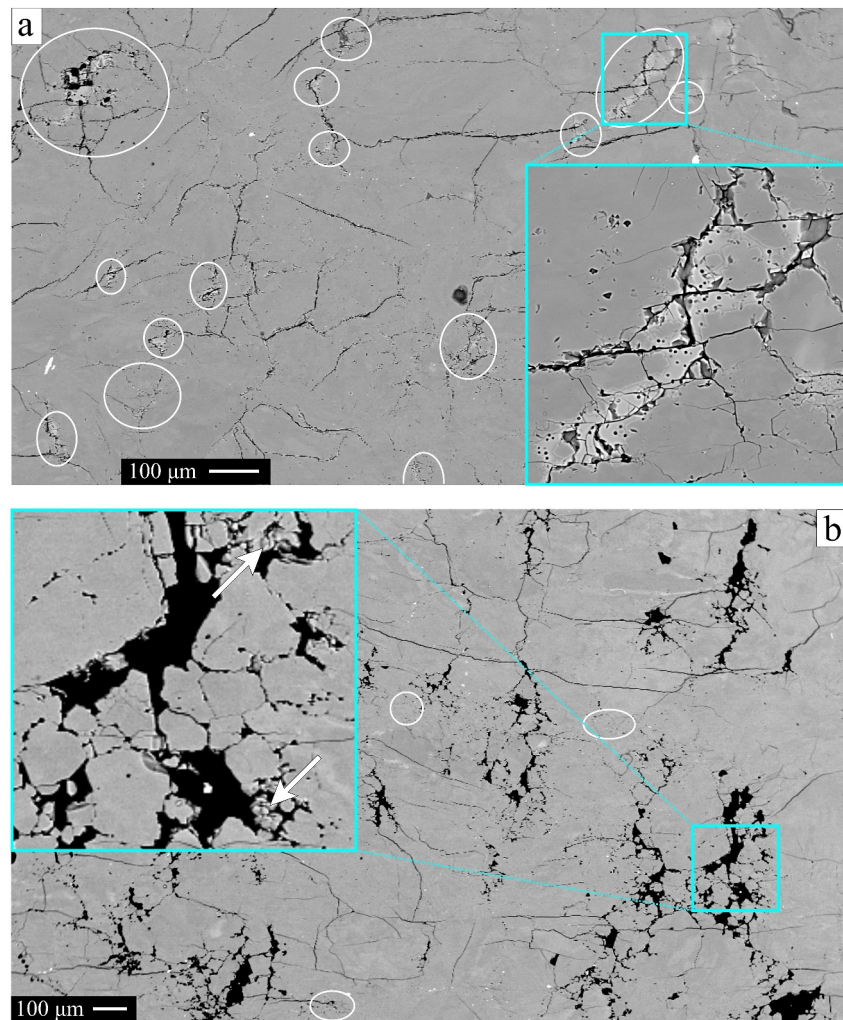


Figure 7. Backscatter electron (BSE) images of the most deformed parts of (a) as-is sample 568PP and (b) 0.5 wt.% H₂O-added sample 569PP, showing prevalence of pockets filled with amorphous matter in (a) (white circles/ellipses) and prevalence of unfilled pockets (b) (black). Amorphous fills show a higher BSE contrast (inset in (a)). Darker parts in the fill are due to surface topography.

and broader cracks (cf. Figures 10a–10c). The cracked regions near the thermocouple are associated with large amorphous pockets (up to 100 μm in size) and newly formed grains with idiomorphic overgrowths (red dashed regions in Figure 10a). The flattened grains in the upper regions of the samples show systems of deformation lamellae that are best visible in the CL maps (pink arrows in Figure 10b). The deformation lamellae formed at small angles to the shortening direction are often bent and/or crosscut by crack networks. In the most deformed region of the strongest sample 565PP, a large proportion of grains is affected by interspersed blue luminescence, revealing dense networks of healed and partly healed cracks (white dashed regions in Figure 10c). These cracks often produce grid-like patterns separating fragments of original grains, while some are recognized as systems of healed step-ladder cracks (white circle and green arrows in Figure 11; Fitz Gerald et al., 1991; Stünitz et al., 2017). EBSD maps show that these domains coincide with very dense networks of low angle boundaries (yellow in Figure 11c) and small misorientations in the original grains. Locally also systems of parallel low angle boundaries coincide with deformation lamellae in the original grains (black ellipses in Figure 11). Locally along boundaries of the original grains, thin zones of very small recrystallized grains can also be observed in these domains (blue arrows in Figure 11).

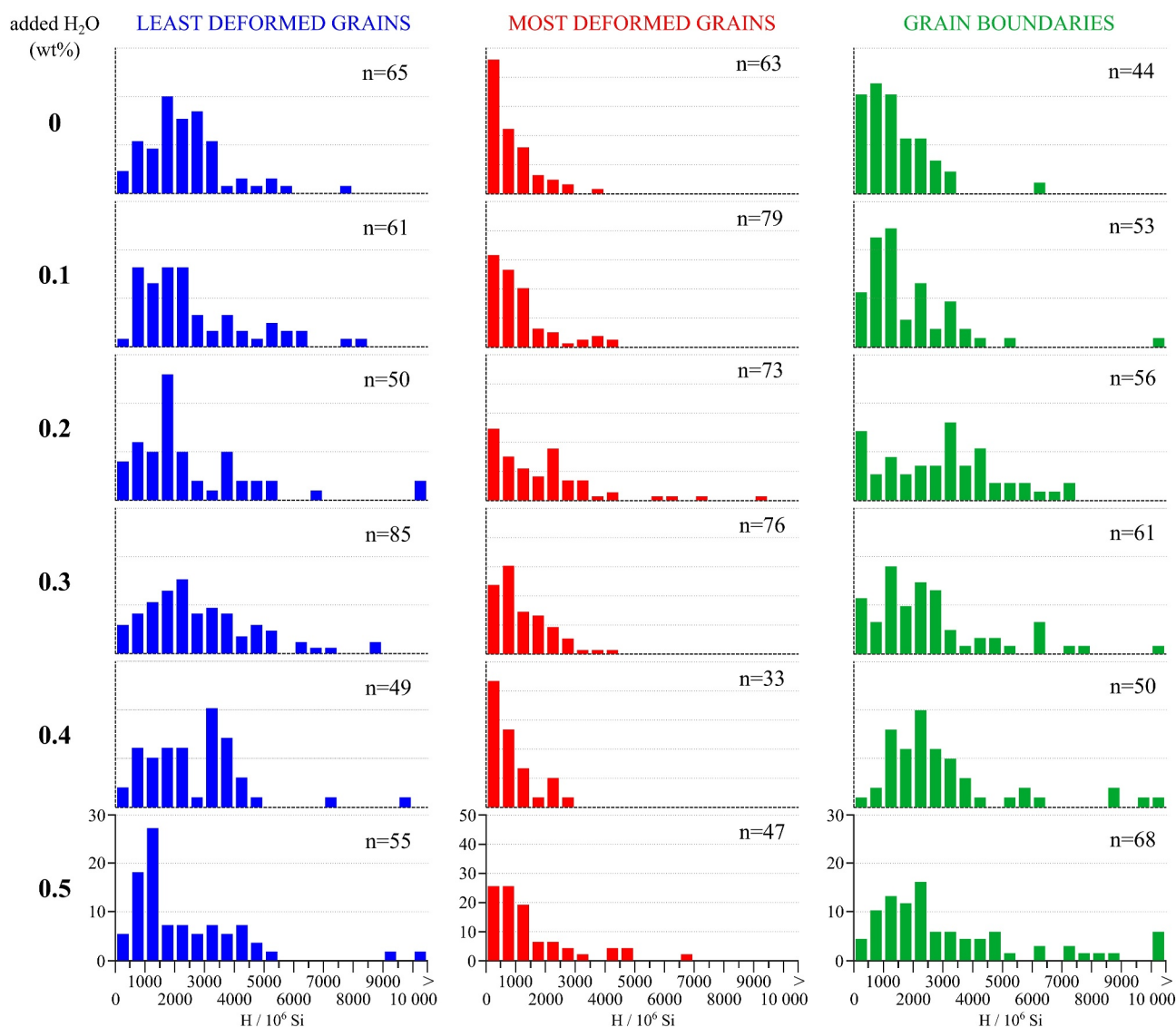


Figure 8. Frequency histograms of H₂O concentrations in the least (blue) and the most (red) deformed grains and the grain boundary regions (green) from all analyzed samples sorted and grouped by quantity of added H₂O. Data are presented as the frequency of H₂O molar concentrations expressed as H/10⁶ Si, calculated using the Beer-Lambert law. Number of measurements is indicated by *n*.

3.6. Strain Analysis and Strain Distribution in the Weaker and Stronger Samples

A particle strain analysis has been performed on the weaker and the stronger sample with 0.4 wt.% of added H₂O (591PP and 565PP, respectively), using the shapes of original sand grains (Figure 12). The sand grain outlines are drawn manually using non-thermionic (“cold”) CL images and evaluated by the grain surface projection method (SURFOR; Panozzo, 1983; Heilbronner & Barrett, 2014; Lexa, 2023). The particle strain has been estimated for sections across the entire samples (bulk strain), as well as separately for the most deformed (most bulged out) and adjacent less deformed regions (red and yellow rectangles in Figures 12a and 12b, respectively). The resulting bulk strain in both samples reached ~25%. This value is only slightly lower than ~30% shortening determined from the mechanical record. Analysis of the starting material shows ~5% anisotropy asymmetrically oriented in the sample (Negre et al., 2021). The orientation of this fabric anisotropy in the starting material with respect to the shortening direction was not determined, due to the lack of systematic features such as bedding in the starting material that could be taken into account during coring. The highest particle strain was determined in the most deformed regions, that is, at the thermocouple level in the weaker sample 591PP and in the upper part of the stronger sample 565PP (cf. red and yellow areas and SURFOR functions in Figures 12a and 12b). Here, the

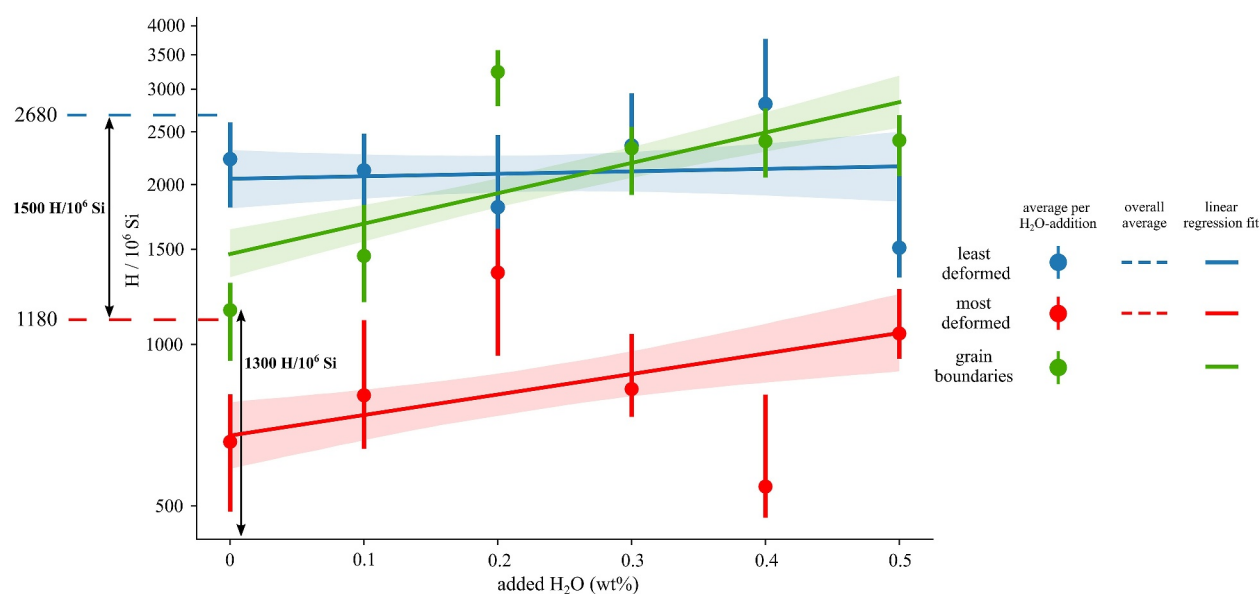


Figure 9. Averages values of molecular H₂O concentrations shown separately for the least deformed grains in blue, the most deformed grains in red, and the grain boundary regions in green. The mean values of measured concentrations are plotted for each H₂O-addition with error bars bootstrapped 95% confidence interval for median (dots). The full lines show the linear regression fit with shaded 95% confidence interval. The horizontal dashed lines mark average concentration from all measurements for the least and the most deformed grains. The y-axis values are ordered in natural logarithm scale.

average particle strains are ~37% for the weaker (591PP) and ~44% for the stronger (565PP) sample. In the less deformed regions, the average particle strain of ~15% is slightly lower in the stronger sample 565PP compared to ~20% of the weaker sample 591PP.

In addition, the cold CL images allow an estimate on the relative amount of quenched melt channels (bright clusters and trails in Figure G1) in the areas with different particle strain in Figures 12a and 12b. The quenched melt from these areas was separated by color thresholding and superposed on the manually redrawn original sand grains (Figure 13). Both regions (with higher and lower particle strain) in the weaker sample 591PP contain a similar amount of visible melt pockets (cf. Figures 13a and 13b), whereas in the stronger sample 565PP, considerably larger amounts of melt are visible in the low strain regions compared to the high strain regions (cf. Figures 13c and 13d). The density of melt pockets in the low strain area of the stronger sample is much higher compared also to both areas from the weaker sample, and it is associated with wider dilatant cracks (cf. Figures 13a, 13b, and 13d; for the original non-thermionic CL images see Figure G1).

3.7. FTIR Maps

The FTIR maps were determined in different regions of sample 597PP, which belongs to the group of stronger samples and has the highest quantity of added H₂O (0.5 wt.%; Figures 2 and 14). The Al-concentrations were measured in the range of 3,313–3,408 cm⁻¹, corresponding to the triplet of discrete Al-absorption bands (Aines & Rossman, 1984; Kats, 1962; Kronenberg, 1994). The Al substitution for Si takes place as a charge compensation for H-incorporation in quartz (forming OH-absorption bands: Si⁴⁺ = Al³⁺ + H⁺). The Al concentrations are higher in the grain boundary regions and cement between original sand grains, so that the outlines of quartz grains can be seen (Figure 14). There is no systematic difference in the Al-content between the upper and lower (near-thermocouple) regions in the sample.

The epoxy and H₂O maps show similar distributions of high concentrations, indicating that most H₂O is measured in epoxy and primarily occurs in epoxy-filled unloading cracks (oriented normal to the shortening direction). In addition to the H₂O in unloading cracks, the maps indicate H₂O in pockets, especially prominent in the region close to the thermocouple. These are arranged in a vertical-array and correspond to the quenched melt material pockets (cf. Figures 7, 13, and 14).

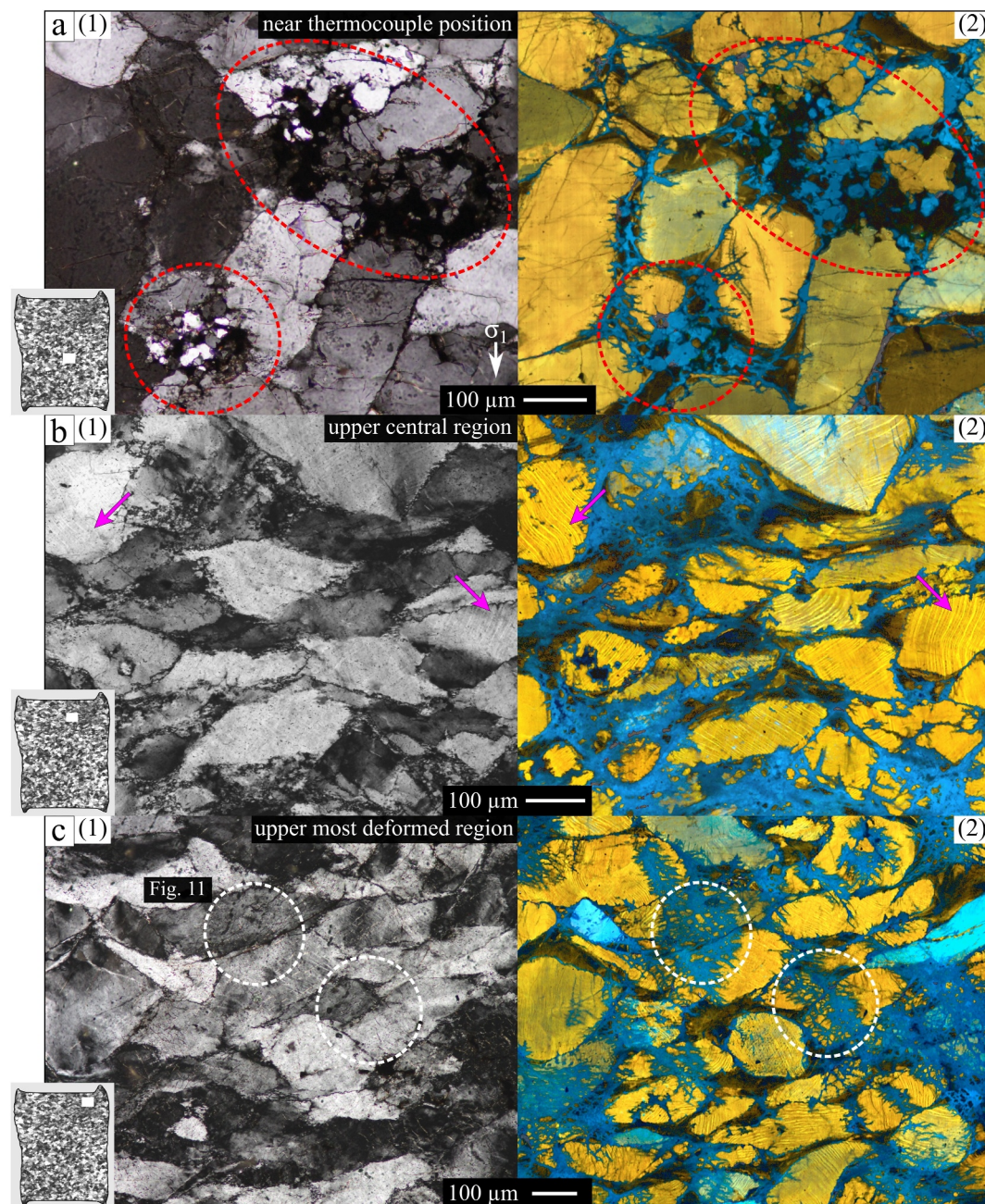


Figure 10. Microstructure of the strongest sample 565PP (0.4 wt.% of added H₂O) (a) at the thermocouple level and (b, c) in its upper more deformed part, shown in (1) cross polarized light and (2) cathodoluminescence. Red circles in (a) mark intensely cracked regions with large amorphous pockets and associated idiomorphic grains. Pink arrows in (b) point to the systems of deformation lamellae. White circles in (c) mark regions of dense networks of healed and partly healed cracks. Area around the upper white circle is explored in more detail in Figure 11.

4. Discussion

Adding H₂O to quartz samples typically results in pronounced weakening (e.g., Griggs, 1967; Griggs, 1974; Hirth & Tullis, 1992; Kronenberg & Tullis, 1984; Post & Tullis, 1998). However, the expected systematic decrease in mechanical strength of quartzite samples with higher quantities of added H₂O is visible only in our low-H₂O-content samples (0–0.2 wt.% added H₂O; Figure 1a). The average stresses recorded between 10% and 30% strain are systematically lower in 0.1 wt.% H₂O-added samples with respect to the as-is ones, while the average stresses for two

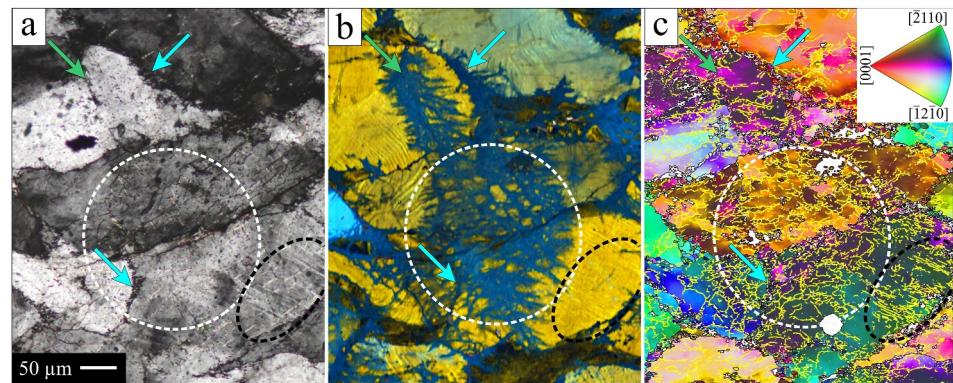


Figure 11. Microstructural features in the most deformed part of the strongest sample 565PP (0.4 wt.% of added H₂O) shown in (a) cross polarized light, (b) cathodoluminescence and (c) electron backscatter diffraction (EBSD) map. Green arrows point to a system of healed step-ladder cracks; blue arrows point to thin recrystallized domains; white circles mark a region of dense networks of healed and partly healed cracks; black ellipses mark a region with low angle subgrain boundaries (LASBs) coinciding with the deformation lamellae. The grains in the EBSD map are colored according to the crystallographic orientation presented in the inverse pole figure scheme related to direction perpendicular to principal stress σ_1 in the sample section; high angle grain boundaries are marked by black, and LASBs by yellow.

0.2 wt.% H₂O-added samples are very similar to 0.1 wt.% added H₂O, although one sample shows progressive hardening toward 30% strain (Figure 1b). Adding more than 0.2 wt.% H₂O (0.3–0.5 wt.%) does not systematically decrease the strength of samples but increases the variability in mechanical strength (Figures 1c and 2). Some 0.3 to 0.5 wt.% H₂O-added samples are substantially stronger than as-is samples. This unexpected observation poses questions about aqueous fluid distribution and its mechanical impact on quartzites.

4.1. Melt and Aqueous Fluid Pockets

In our samples, we distinguish pockets filled with amorphous matter and unfilled (empty) pockets (cf. Figures 7a and 7b). Bureau and Keppeler (1999) have determined the critical points for different silicate melt-H₂O systems, while for a haplogranitic system (a melt composition closest to mica + quartz, i.e., the one appropriate for sheet silicate breakdown in our samples; see in Appendix C) at 900°C and 1 GPa (below their critical point), two

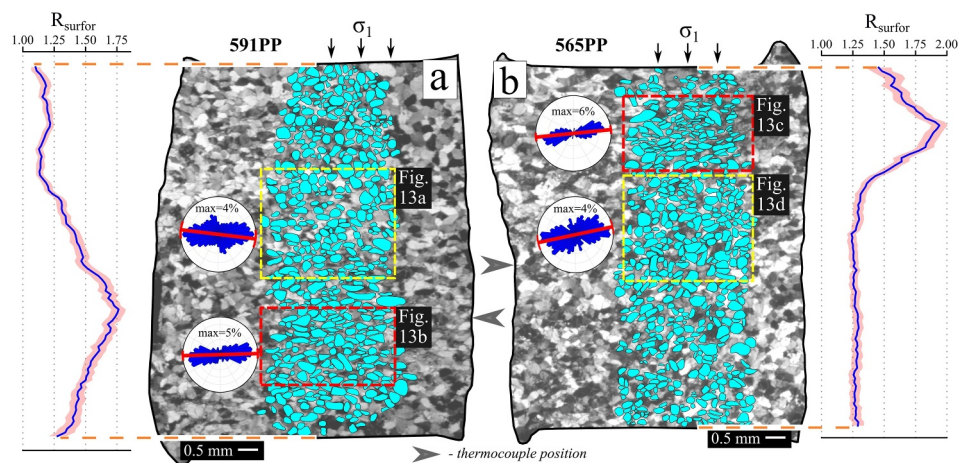


Figure 12. Cross-polarized scans of (a) the weaker 591PP and (b) the stronger 565PP 0.4 wt.% H₂O-added samples with digitized original sand grains in light blue. Red rectangles include grains in the most deformed (bulged out) regions and the yellow rectangles in the adjacent less deformed regions. The corresponding rose diagrams show preferred orientation of the sand grains (blue sectors in 5-degree-intervals) in these regions, with a labeled maximum proportion of the outermost circle. The areas marked by the rectangles are shown in Figures 13 and G1. Strain along the digitized strips is calculated as the ratio between maximum and minimum of the SURFOR function of the individual grains. The red shaded error is determined as ± 1 sigma (bootstrapped).

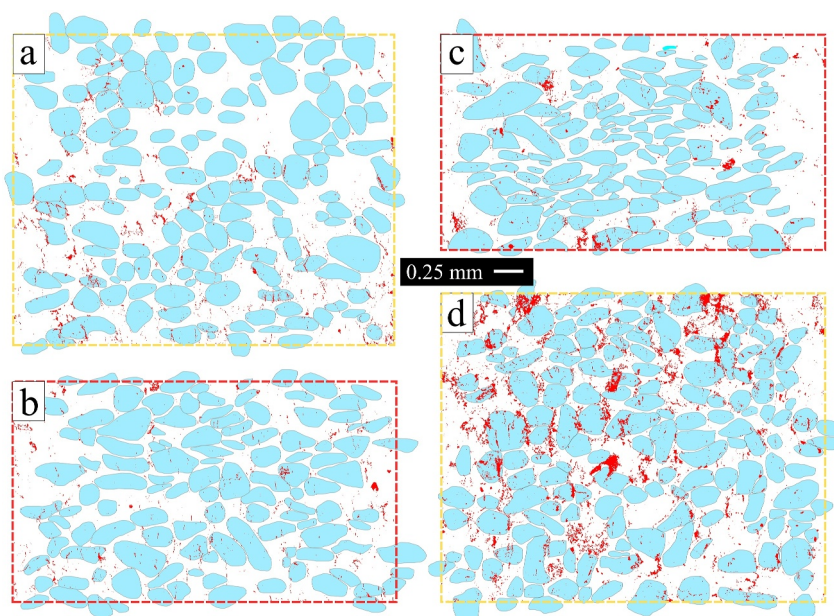


Figure 13. Digitized original sand grains from the strain-analyzed regions marked by rectangles in Figure 12 (light blue) and channels and pockets filled with amorphous matter (red), extracted from the non-thermionic cathodoluminescence (CL) images by color thresholding. The images in (a) and (d) show the areas with lower, and in (b) and (c), with higher particle strain, in (a, b) the weaker sample 591PP and (c, d) the stronger sample 565PP (see Figure 12). Original non-thermionic CL images are presented in Figure G1.

individual melt/fluid phases develop. There is (a) a silicate melt and (b) an aqueous fluid. From the microstructures and the composition determined for the amorphous matter that fills the pockets, associated with spherical pores (inset in Figure 7a), it is inferred that the amorphous material corresponds to quenched melt with bubbles of exsolved vapor phase (see Figure 8e in Pongrac et al., 2022) formed during rapid quenching (Bureau &

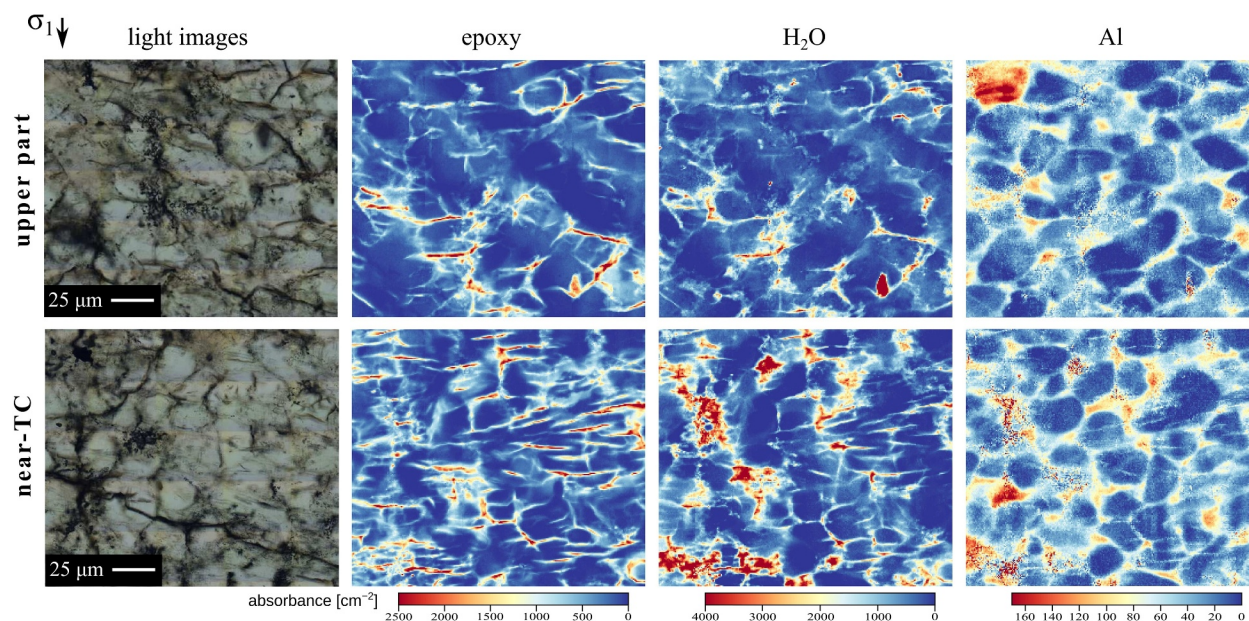


Figure 14. Fourier-transform infrared spectroscopy maps showing concentration distribution of epoxy, molecular H₂O and Al, in the stronger 0.5 wt.% H₂O-added sample 597PP. The upper and lower maps were scanned in the high bulk strain top region, and the low bulk strain near-thermocouple region of the sample, respectively. All concentrations are expressed as Integrated absorbance in cm⁻². The color variation forming diagonal bands visible mostly in the upper part maps are artifacts resulting from interference effects due to small thickness variations within the sample. Shortening direction is indicated in the upper left corner.

Kepler, 1999; Manning, 2004; Ni et al., 2017). The unfilled pockets in Figure 7b, on the other hand, are interpreted to correspond to pockets originally filled with an aqueous fluid during the experiment. In the high-H₂O samples (Figures 5c–5e), we observe a larger amount of aqueous fluid pockets with only minor patches or rims of melt around the margins of cracks (inset in Figure 7b). Their occurrence is especially pronounced in the 0.5 wt.% H₂O-added sample, whereas in the low-H₂O samples (especially as-is), the pockets are dominantly filled with quenched melt (Figure 7a). As the melt has been generated by break-down of accessory phyllosilicates (Pongrac et al., 2022), its production is limited by the initial low amount of the phyllosilicates (<1%). As the generated melt can absorb up to ~11 wt.% of total available H₂O (Appendix C), all excess H₂O that cannot be dissolved in the melt will produce aqueous fluid pockets. Thus, with addition of more H₂O, a larger portion of aqueous fluid pockets develops in the samples (Figures 5c–5e; cf. Figures 7a and 7b). During thin section preparation, the H₂O from the aqueous fluid pockets is removed, leaving empty pores.

4.2. Deformation and Distribution of H₂O

4.2.1. Decrease in H₂O Content of Quartz Grains

The average content of ~1,000 H/10⁶ Si in strongly deformed grains does not show much variation for different amounts of added H₂O and appears to represent a typical average H₂O-content of deformed quartz grains (red dashed line in Figure 9). These values are similar to the values measured in samples deformed at similar conditions: ~800 H/10⁶ Si (Post & Tullis, 1998) and 640–1,530 H/10⁶ Si (in porphyroclasts; Palazzin et al., 2018). The relatively low H₂O concentrations in the strongly deformed grains with respect to the less deformed ones and the starting material indicate that part of the initially present H₂O content is released from the original grains during application of high *P* and *T* conditions and further deformation (Figures 8 and 9). Similar results have been already reported from the experiments of Post and Tullis (1998), Stipp et al. (2006), and Stünitz et al., 2024. In the latter study, the two steps of (a) application of *P* and *T* and (b) subsequent deformation are discriminated, and it is shown that a large proportion of the water loss from grain interiors occurred during phase (a). The present study further adds the information that the water loss is independent from the amount of water added to the experimental samples.

The majority of the initial H₂O in original grains is present in the form of fluid inclusions. The decrepitation of these fluid inclusions, through the formation of a network of microcracks, is presumably the main factor to account for the H₂O loss in the grain interiors during application of *P* and *T* and deformation (cf. Palazzin et al., 2018; Stünitz et al., 2017; Tarantola et al., 2010, 2012). Here, penetrative cracking is demonstrated by CL imaging and the reprecipitation of a CL-bright quartz in crack network (dark blue in Figures 10 and 11).

The process of cracking and decrepitation of fluid inclusions, accompanied by a transfer of part of the water from a grain interior toward the surrounding medium, may also have some consequences for grain crystal plastic deformation. Following decrepitation, crack healing creates new smaller inclusions and clusters, producing more potential sources for generation and multiplication of dislocations (Fitz Gerald et al., 1991; McLaren et al., 1989; Morrison-Smith et al., 1976; Stünitz et al., 2017; Tarantola et al., 2012).

4.2.2. Storage of H₂O Within Grain Boundaries

The amount and speciation of water present along the GB during deformation is much more difficult to estimate than in grain interiors. Our FTIR measurements of the grain boundary domains include, in addition to a grain boundary itself, a large contribution from the volume of quartz crystal. In addition, there is hardly any guarantee that the grain boundary system, including the water stored, remains unperturbed during the sequence of operations from HP-HT conditions to FTIR measurements. Significant gains or losses may occur during quenching or during thick section preparation. Hence our measurements of water content in volumes that include GB have to be considered with care. Nonetheless, we observe a systematic increase in the amount of water stored in the grain boundary regions with increasing amount of added water. This supports the assumption that the experimental system is closed, at least with respect to water content, during deformation and further sample treatment.

In addition, our observation of two distinct microstructures in the grain boundary regions, the HCD and LCD, may provide information on the water storage capacity of the GB. On average, ~1,500 H/10⁶ Si (equivalent to 0.02 wt.% H₂O) were released from the original grains during deformation, as can be estimated from the difference between average values of all H₂O content measurements in the least and in the most deformed grains (blue and red dashed

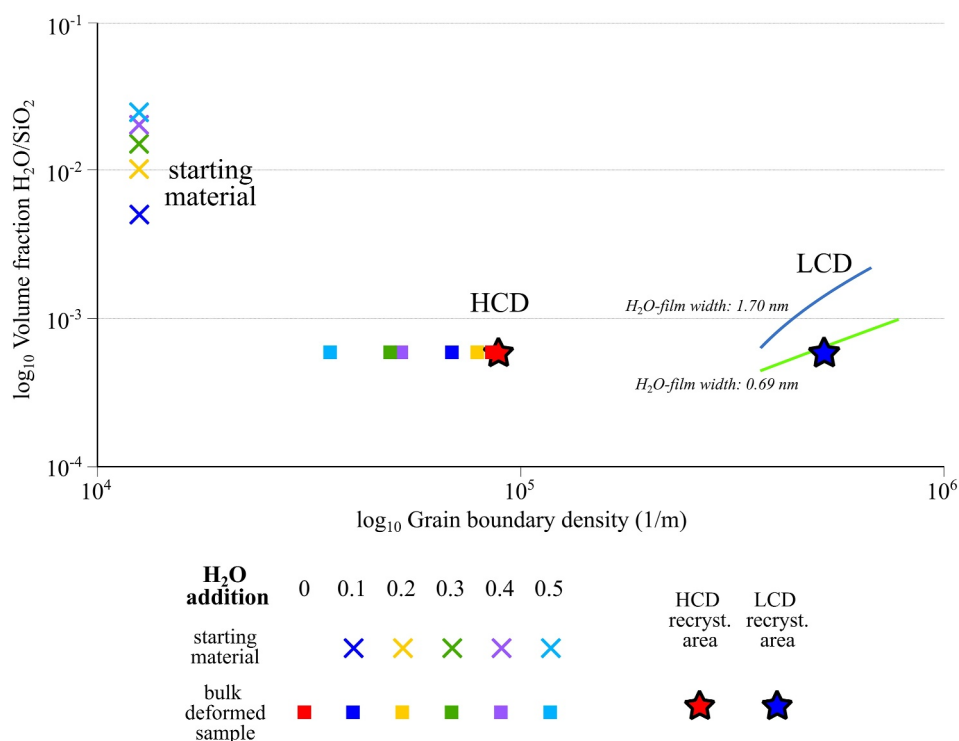


Figure 15. Volume fraction of H₂O versus grain boundary density in the samples with different content of added H₂O. Results are shown separately for the proportion of added H₂O to the samples before deformation (with grain boundary density of the starting material; crosses), and for the average H₂O content that is released from the grain interiors during the deformation to the grain boundary region (1500 H/10⁶ Si; see Figure 9) in deformed samples. For the deformed samples, results are shown for the bulk deformed samples (squares), high crack density (HCD) domains (red star) and low crack density (LCD) domains (blue star). Grain boundary density was calculated separately for HCD and LCD domains from the electron backscatter diffraction maps, assuming the same density in HCD and LCD domains in all samples. Grain boundary density for the bulk deformed samples is estimated according to proportion of least deformed parts, LCD and HCD domains for each sample. Results are compared with the regression lines that represent average thicknesses of H₂O-film along the boundaries, where the upper (blue) regression line represents oversaturation of the boundaries (from Palazzin et al., 2018).

lines in Figure 9). Assuming that the system is closed, the water released from a grain is transferred to the grain boundary region. The geometry and distribution of the grain boundary water is a debated subject (Den Brok, 1998; Farver & Yund, 1992; Ito & Nakashima, 2002; Nakashima et al., 1995), however in any case it scales with the grain boundary density, that is, the grain boundary area per volume. Using an assumption of a thin water film wetting all GB, the grain boundary density and total water content along boundaries can be related through a single parameter, namely the grain boundary width. Such estimate was attempted in Figure 15, for LCD and HCD domains, considering that the total water content corresponds to the amount released from the deformed grains. The resulting calculation suggests that GB in LCD regions can accommodate all H₂O released from the neighboring grains through an H₂O-film thickness of ~0.7 nm. Note that such a value is only a calculated number of a nominal width and might not correspond to a true grain boundary width. The compilation done for natural rocks by Ito and Nakashima (2002) concluded an average film thickness of ~10 nm, while recent high pressure experiments in Griggs-type apparatus on synthetic quartz aggregates estimated values between 0.7 and 1.7 nm (Palazzin et al., 2018). In spite of these large uncertainties, it appears that in contrast to the HCD domains, the GB in LCD domains have a sufficient capacity to store all water released by the deformed grains. This conclusion, based on simple assumptions and H₂O budget calculations, matches the observation that the LCD regions show rare pores or cracks. On the contrary, the HCD regions contain abundant pores and cracks suggesting an excess of H₂O beyond the storage capacity of the grain boundary film.

4.3. Deformation and Strain Localization

Two types of deformation are observed in all samples: (a) Cracking and (b) crystal plastic deformation. Even though brittle deformation, that is, cracking and subsequent grain fragmentation, becomes more dominant with the addition of H₂O (Figures 6 and B1), it does not significantly contribute to the sample strain. These aspects are discussed in Negre et al. (2021) and Pongrac et al. (2022), concluding that the cracks do not show any offset nor coalesce to form larger brittle deformation zones. Also, the total volume fraction of cracks in as-is and 0.1 wt.% H₂O-added samples is very low (Pongrac et al., 2022). Here we demonstrate that, even in the 0.4 and 0.5 wt.% H₂O-added samples, where the total volume fraction of cracks is highest, the bulk strain still is mainly produced by crystal plasticity, that is, grain flattening, as demonstrated by particle strain analysis in Figure 12. As inferred in Pongrac et al. (2022), the crystal plasticity of the original grains is accommodated mainly by dislocation creep, operating in parallel with dissolution precipitation and grain boundary sliding as accommodation mechanisms for strain incompatibilities.

In all weaker samples, the most deformed regions are located near the thermocouple level, where the temperature is expected to be highest (Figure 2a; Pec et al., 2016). In the stronger samples the regions of the highest strain occur in the upper parts of the samples, where the temperature is estimated to ~5–8% lower with respect to the thermocouple position (Cionoiu et al., 2022; Pec et al., 2016). In the upper part (maximum strain) of the strongest sample 565PP (0.4 wt.% H₂O added), with the lowest α -angle (Figure 2), cracking, recrystallization (HCD), and plastic strain are observed, manifested by domains of dense step-ladder and distributed crack systems and flattened original grains with pronounced deformation lamellae (Figures 10b, 10c, and 11). However, dilatant cracks and pockets with melt or aqueous fluid appear only scarcely (Figures 13c and G1). In the least deformed parts at the thermocouple level, crystal plastic deformation is virtually absent, but many wide dilatant cracks and pockets are observed (Figures 10a, 13d, and G1).

The “cold” CL images of the weaker and stronger 0.4 wt.% H₂O-added samples (Figures 13 and G1), revealed important differences in quantity and distribution of dilatant cracks. In the weaker sample (591PP), the amount of melt and aqueous fluid pockets is similar in both the most deformed and adjacent regions (Figures 13a and 13b). In the stronger sample (565PP), the melt- and aqueous fluid- filled cracks and pockets are significantly more abundant in the region that is not plastically deformed, whereas the plastically deformed region shows a low density of the cracks and pockets (cf. Figures 13c and 13d). A similar distribution of dilatant cracks is observed in the FTIR maps of sample 497PP (Figure 14). Thus, it is conceivable that the mechanical behavior of samples with more than ~0.2 wt.% of added H₂O depends on the amount of mode-I dilatant cracks formed presumably during early stages of deformation (Pongrac et al., 2022) and/or at later stages (Vollbrecht et al., 1999). These cracks may drain fluid from grain boundary regions into aqueous fluid or melt pockets. If GB are depleted in aqueous fluid, dissolution precipitation processes are expected to be less efficient, so that grain boundary sliding and/or grain boundary migration processes may be inhibited. Such draining processes could result in a hardening effect by dilatancy (e.g., Beeler et al., 2016; Fischer & Paterson, 1989; Renner et al., 2000), which may cause a greater heterogeneity in deformation and variability in strengths of the samples. Dilatancy hardening denotes the process where cracks form faster than the pore fluid can flow into the dilating cracks, so that the pore pressure in cracks is reduced, causing the cracks to be arrested and material to be ultimately strengthened due to increased effective pressure (Brace & Martin, 1968; Brace et al., 1968; Hirth & Beeler, 2015; Olgaard et al., 1995; Renner et al., 2000). The dilatancy effect envisaged here is different: the dilatant axial cracks are filled with melt or aqueous fluid, draining the surrounding volume of the sample of fluid, as previously inferred by Schmocker et al. (2003). With a very small amount of pore fluid present at the high confining pressure and temperature of these experiments, drainage of the fluid from the grain boundary regions can be very efficient as demonstrated by the pockets filled with aqueous fluid and melt (Figures 7 and 13).

If the fluid drainage from GB is most efficient in the hottest region of the sample (in the vicinity of the thermocouple position), the crystal plastic deformation may be less efficient due to suppressed dissolution-precipitation, which is inferred to act as a serial process in combination with dislocation glide as an accommodation process in dislocation creep (Ghosh et al., 2022; Nègre et al., 2021; Pongrac et al., 2022; Stünitz et al., 2024). Crystal plastic deformation may then take place in other parts of a sample instead. If the

crystal plastic deformation takes place in regions with lower temperature (farther from the thermocouple position), the sample strength is expected to be higher. Such an effect may explain the observations of stronger samples being more deformed in the upper regions than at the thermocouple level (Figures 1 and 2). As the location of fluid drainage may vary within the sample, the distribution of plastically deformed regions will also vary depending on the fluid content in the grain boundary regions. Whether the plastic strain takes place in warmer or colder regions of the sample, the bulk sample strength will then depend on the distribution of fluid drainage, resulting in more variable sample strengths with more H₂O added and thus larger variability of drainage regions.

The phenomenon of the “inverse” strain distribution is not observed in the samples with lower quantities of added H₂O, probably due to much less extensive H₂O-promoted cracking, and insufficient storage space to drain the GB. The fact that Kronenberg and Tullis (1984) did not observe differences in the mechanical behavior with up to 0.5 wt.% of added H₂O may be due to the considerably larger grain boundary surface area in the very fine grained novaculite used in their experiments, because the storage capacity of such a material is orders of magnitude higher than that of the coarse grained material used in this study (novaculite with added H₂O of up to 0.5 wt.% plots near the region of the LCD points in Figure 15a).

4.4. The Effect of Pore Fluid Pressure

The studies of Hirth and Beeler (2015) and Beeler et al. (2016) demonstrated that pore space connectivity, in an inversely proportional relationship with real contact area of grains/asperities, defines the values of the effective stress coefficient, and thus also the dependence of effective stress on pore pressure. For brittle deformation, such as frictional sliding, the real contact area between grains is small, pore space connectivity is high, resulting in effective pressure coefficient values close to 1 ($\sigma_e = \sigma - \alpha P$; where α is the effective pressure coefficient) and effective stress will be smaller than the applied normal stress by the value of pore fluid pressure (Beeler et al., 2016; Handin et al., 1963; Hirth & Beeler, 2015; Morrow et al., 1992; A. M. Thomas et al., 2012). For ductile deformation at elevated temperatures, where the grain contact area increases due to plasticity, pores become isolated and high pore pressures near or at the lithostatic value are expected. For this condition, the effective stress would tend toward 0. In order to explain rock strength at realistic levels, effective pressure coefficients near 0 need to be invoked (Beeler et al., 2016; Dieterich & Kilgore, 1996; Hirth & Beeler, 2015; A. M. Thomas et al., 2012).

Fluid/melt pockets in our samples can be inferred to represent sites of high pore fluid pressure, satisfying condition $P_{\text{fluid}} \approx P_{\text{lithostatic}}$. However, the criterion $P_{\text{fluid}} \approx P_{\text{lithostatic}}$ alone is insufficient to infer mechanical instability of the material, but the volume fractions of fluid/melt pockets in addition to the local pore fluid pressure need to be considered. Since in our case the fluid/melt pockets are not connected on a sample scale, these domains, even though creating local pore pressures satisfying $P_{\text{fluid}} \approx P_{\text{lithostatic}}$, do not lower the material bulk strength. The main reason for this most likely is the small fluid volume and insufficient crack connectivity (Beeler et al., 2016; Hirth & Beeler, 2015; A. M. Thomas et al., 2012). Menegon et al. (2011) also did not observe any influence of melt on mechanical strength in migmatitic gneisses, even with a melt content of ~5% vol. Inferring the melt-fluid fraction of up to ~4% (locally) in our 0.5 wt.% H₂O-added samples, we demonstrate that such a melt-fluid fraction is insufficient to produce bulk weakening, which requires a re-evaluation of critical melt percentage discussed by Rosenberg and Handy (2005).

In any case, a heterogeneous distribution of H₂O is observed in all samples. Such heterogeneity is not expected given the supercritical state of H₂O under conditions of 900°C and 1 GPa, where a homogeneous distribution of H₂O on the sample scale would be expected.

4.5. Application to Natural Deformation

H₂O is a very important weakening agent for crystal plastic deformation of quartz and other silicates (Chopra & Paterson, 1984; Griggs, 1967; J. Tullis and Yund, 1980, 1989). The application of experimental results of the role of H₂O in quartz deformation to the natural situation is not necessarily straightforward because of the differences in pressure, temperature, and strain rate conditions. Kronenberg et al. (1990) have concluded that microcracking can lead to fluid infiltration into shear zone, causing H₂O weakening of quartz and feldspar, based on FTIR measurements of H₂O in natural shear zones that show higher H₂O contents than the undeformed country rock (see also Gleason & DeSisto, 2008). The difficulty of volume diffusion of H₂O into

quartz (Gerretsen et al., 1989; Kronenberg et al., 1986) certainly makes advective fluid infiltration through (micro)cracking and crack healing the most probable mechanism for H₂O to enter quartz crystals (Fitz Gerald et al., 1991; Kronenberg et al., 1986, 1990; Palazzin et al., 2018; Stünitz et al., 2017; Tarantola et al., 2010, 2012). Recently, and differing from earlier results, Kronenberg et al. (2020) have demonstrated that the most strongly deformed and most completely recrystallized portions of the sheared quartzite below the Moine thrust contain lower H₂O contents than the undeformed country rock. Very detailed synchrotron FTIR analyses of material from different naturally deformed quartzites indicate highly variable H₂O contents within individual grains (Kronenberg et al., 2017). Thus, H₂O contents of naturally deformed quartz crystals can vary considerably, although there appears to be a general trend that H₂O contents tend to decrease with temperature of deformation (Ito & Nakashima, 2002; Nakashima et al., 1995). As shown here, intra-grain H₂O contents of ~1,000 H/10⁶ Si are sufficient to facilitate crystal plastic deformation (dislocation glide with some recovery) in quartz, consistent with earlier determinations and literature reviews of several hundred ppm of OH in experiments by Jaoul et al. (1984), Paterson (1989), and Kronenberg (1994) and ~320 H/10⁶ Si in natural rocks (Gleason & DeSisto, 2008). However, it is important to note that our H₂O concentrations would be approximately half of the reported value if they are evaluated the same way as in the mentioned studies, after Kats (1962) and Paterson (1982). Kilian et al. (2016) found very low H₂O contents (10–360 H/10⁶ Si) in deformed quartz grains, which have been drained of H₂O during deformation by grain boundary migration. It is discussed whether re-hydration of grains by microcracking and crack healing is required or whether even such low H₂O contents are sufficient to facilitate quartz deformation in nature (Kilian et al., 2016). In any case, the observed intra-grain decrease in H₂O content during deformation does not present an instance of hardening of quartz during deformation as speculated by Finch et al. (2016). Generally, modification of H₂O contents in natural rocks by later processes such as exhumation, cracking, etc. need to be considered, so that care needs to be taken in the interpretation of natural rocks.

As shown here, the H₂O drained from crystals can stay in the grain boundary region, as observed previously by Post and Tullis (1998) and Ito and Nakashima (2002). The grain boundary fluid film may help to facilitate dissolution precipitation and grain boundary sliding processes (cf. Ghosh et al., 2022; Nègre et al., 2021; Pongrac et al., 2022; Stünitz et al., 2024). To promote natural quartz deformation by plasticity it appears crucial that the grain boundary fluid is not drained from the rock by, for example, partial melting (Kohlstedt et al., 2000; Mackwell et al., 1985; Seaman et al., 2013). The partial melt will dissolve the aqueous fluid and may effectively dry the GB and by this process lead to a strong lower crust (Menegon et al., 2011). The effect of local draining aqueous grain boundary fluid into dilatant cracks and pockets has been demonstrated here by the formation of fluid or melt-filled pockets due to axial cracking and dilatancy. Such local drainage of fluid seems to be caused by high pore fluid pressure and an over-saturation of the storage capacity of GB. Such an induced heterogeneity in fluid distribution has mechanical consequences, at least on the local scale. It is unclear to what extent such local effects may affect rock strength, mainly because naturally deformed examples always preserve a time-integrated picture of the whole deformation history, where local effects are unlikely to be preserved.

Fluid- or melt-filled pockets as a consequence of oversaturation of the grain boundary storage capacity have also been observed in the form of Riedel shear bands in shear experiments by Schmocker et al. (2003) and Palazzin et al. (2018). For high H₂O contents (1.3 wt.%), pervasive Riedel shear bands cause hardening of the quartz material (Schmocker et al., 2003), but for low H₂O contents of up to 0.3 wt.% no mechanical effect has been observed (Palazzin et al., 2018). Low H₂O contents of up to 0.5 wt.% appear to be more applicable to metamorphic low to medium grade conditions (Ito & Nakashima, 2002; Nakashima et al., 1995), where quartz deforms by crystal plasticity in nature. In this study we observe more variable mechanical behavior above H₂O contents of ~0.2 wt.%, but our samples have been deformed in axial compression, not in shear. Geometrically, shear bands are expected to distribute fluid during deformation rather than just store it like the axial crack-pockets, because the tips of shear bands tend to deflect into the shear plane. Thus, local H₂O drainage (i.e., hardening) effects as observed in this study may become important in shear (typical for natural deformation) only at higher H₂O contents, as found in Schmocker et al. (2003).

5. Conclusions

The addition of more than 0.2 wt.% H₂O to deforming samples at high temperatures and confining pressures leads to a more variable mechanical behavior of the samples, that is, weakening and strengthening. The strengthening of

the samples results from strain localization by crystal plastic deformation in the upper parts of the samples, where the temperature is lower compared to the thermocouple position. The strain localization most likely results from dilatant cracks and melt or fluid filled pockets that develop during deformation. If the dilatancy effect is sufficient, the fluid is drained from the grain boundary space into open cracks and pockets, causing dissolution-precipitation processes to be impeded. Dissolution precipitation processes and grain boundary sliding are important accommodation processes acting in series with dislocation glide during crystal plastic deformation (surface-processes-accommodated dislocation creep) that produce bulk sample strain. Mode-1-cracking, although common in the samples, especially at higher H₂O contents, does not contribute significantly to sample strain.

The greater part of H₂O that is initially present in the original grains is released into the grain boundary region during deformation. The added H₂O is also accumulating in the grain boundary regions. With more added H₂O, the H₂O over-saturation of grain boundary space becomes more intense, leading to more abundant dilatant cracks. In the low crack density LCD domains where the recrystallization is governed by subgrain rotation, the amount of H₂O in the grain boundary space is below the saturation limit.

Even though the H₂O content of up to 0.5 wt.% creates local pore pressures satisfying criterion $P_{\text{fluid}} = P_{\text{lithostatic}}$, it does not necessarily lower the quartzite strength because offset on the mode-1-cracks is virtually absent and there is no connectivity of the cracks on the sample scale. We demonstrated that a melt-fluid fraction locally up to ~5% in the 0.5 wt.% H₂O-added samples is insufficient to produce bulk sample weakening, which requires re-evaluation of critical melt percentage for weakening proposed by Rosenberg and Handy (2005).

Appendix A: Treatment and Evaluation of FTIR Data

The amount of molecular H₂O was determined after the calibration of the integral absorption band between ~3,000 and ~3,800 cm⁻¹ using Beer-Lambert law (e.g., Gleason & DeSisto, 2008; Paterson, 1982):

$$A_i = C \cdot t \cdot \epsilon,$$

where A_i is integrated absorbance (cm⁻¹), C is molar concentration of H₂O in the sample expressed as H/10⁶ Si, ϵ is wavelength-dependent molar absorptivity coefficient (mol⁻¹ cm⁻¹) and t is thickness of the sample (cm). For obtaining C (concentration) values, the calibration of Aines and Rossman (1984) was used:

$$C (\text{H} : 10^6 \text{Si}) = A_i/t \cdot 1.05.$$

This calibration makes the H₂O concentration values comparable to the results of previous studies (e.g., Kronenberg & Wolf, 1990; Kronenberg et al., 1990; Post & Tullis, 1998). Since the broad band absorption due to molecular H₂O is isotropic (Aines et al., 1984; Libowitzky & Rossman, 1997; Stalder, 2021), the values of the measurements were normalized following S. M. Thomas et al. (2009). The molar H₂O concentrations were converted into weight proportions H₂O/SiO₂ using the relationship H₂O:SiO₂ (wt ppm) = 6.67 H:10⁶ Si. Based on the calibration of the microscope stage and the stability of its rack and pinion, the error in determination of thickness of the thick sections is estimated to be ±5 μm.

Transmission Fourier-transform infrared spectroscopy (FTIR) analyses for mapping were carried out at the Institute of Geological Sciences of the University of Bern using a Bruker Tensor II spectrometer with a global infrared source and a KBr beam-splitter, coupled to a Bruker Hyperion 3,000 microscope with a dry air-purged sample chamber. The instrument is equipped with a focal plane array (FPA) Detector with 64 × 64 = 4,096 liquid nitrogen cooled MCT elements on a square array with a pixel size of 2.7 μm × 2.7 μm. A 2 × 2 binning was used resulting in a 5.4 × 5.4 μm pixel resolution, higher signal quality and an improved signal to noise ratio. Spectra were acquired with 8 cm⁻¹ wavenumber resolution and 128 scans between 900 and 3,850 cm⁻¹.

A1. Data Treatment and H₂O Content Determination

To apply the Beer-Lambert law, the spectra were first corrected by the “rubber band” method (Pirzer & Sawatzki, 2006), used to obtain a flat baseline. The absorbance of H₂O was then determined in the wave number region 3,000–3,800 cm⁻¹. The Araldite® epoxy (inadvertently used for the thick section preparation) contains

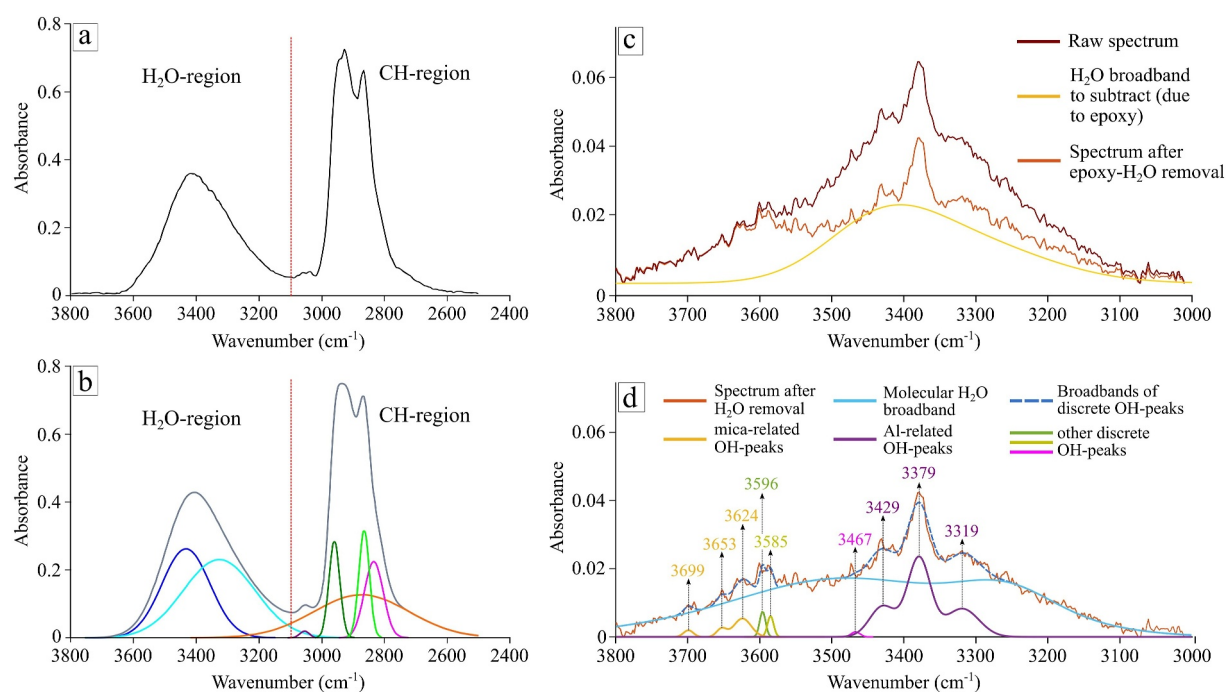


Figure A1. (a, b) Example of an IR absorption spectrum of the Araldite[®] epoxy in the wavenumber range 3,800–2,400 cm⁻¹ (baseline corrected), composed of H₂O absorption broadband in the region 3,800–3,100 cm⁻¹ band and of CH-absorption peaks in the region 3,100–2,600 cm⁻¹: (a) raw spectrum; (b) smoothed fit (gray) deconvoluted to 8 Gaussian curves (in colors). (c, d) Example of a quartz spectrum (measured on a least deformed grain in sample 588PP) showing (c) the raw spectrum (dark red) before the subtraction of overestimated H₂O due to the epoxy (yellow), and the resulting spectrum after H₂O subtraction (orange), and (d) deconvolution of the corrected spectrum into Gaussian curves representing molecular H₂O broadband (light blue) and discrete OH-peaks (in different colors).

H₂O, so that some of the measured spectra showed H₂O absorption signal from both the investigated quartzite samples and the epoxy. For this reason, the epoxy contamination was separated and subtracted from the examined wave number region of the spectra, by using a correction procedure, developed as a set of in-house developed Matlab scripts (Stünitz et al., 2024).

After subtracting the epoxy contamination, the quartz spectra were deconvoluted into a sum of Gaussian curves. These had separated molecular H₂O from discrete OH peaks (Figures A1c–A1d). Two broad Gaussian curves corresponding to the symmetric and asymmetric stretching bands of molecular H₂O (located at 3,280 and 3,490 cm⁻¹, respectively) were used to simulate the broad band of H₂O absorption centered at around 3,400 cm⁻¹. The list of the discrete OH-peaks deconvoluted from the raw broadband is provided below. Separate OH-peaks were selected according to Kats (1962), Aines and Rossman (1984), Kronenberg et al. (1986), Niimi et al. (1999), Stünitz et al. (2017), and Jollands et al. (2020).

Each of the measured spectra was deconvoluted into molecular H₂O broadband and discrete OH-peaks in the same way (Figure A1d). For the selected Gaussian curves, their height, width and the integrated area have been calculated. To decrease the error of the baseline correction, spectra with detectable interference were eliminated from the data set.

A2. Removal of the Epoxy Contamination

Epoxy is normally identified by the CH bands in the wavenumber region 3,100–2,600 cm⁻¹ with two principal peaks at ~2,931 and ~2,869 cm⁻¹ (Figure A1a), while these bands are absent in quartz spectra. In order to establish a model of the relation between CH- and H₂O-broadbands resulting from the epoxy, FTIR measurements were conducted on pure Araldite[®] epoxy samples (Figure A1a). After the baseline correction, the H₂O and CH bands of the mean epoxy spectrum were deconvoluted in a sum of Gaussian curves, allowing to quantify and establish a smooth relationship between H₂O and CH bands of epoxy IR spectrum (Figure A1b). Within the deconvolution method, the positions of half-widths of the eight Gaussian curves were obtained from the epoxy

mean spectrum in the range 2,500–4,000 cm^{-1} . In the second step, the heights of the obtained Gaussian curves were adapted according to their positions and half-widths.

After the deconvoluted model of epoxy IR spectrum is established, a relationship between the H_2O and CH bands allows quantification of the epoxy-related H_2O . This used the half-height between CH peaks at 2,860 and 2,960 cm^{-1} . Due to slight variations in position and shape of the major peaks, their half-heights were chosen as a more reliable parameter.

In the measured spectra of quartzite samples, the epoxy-related H_2O in the region of 3,000–3,800 cm^{-1} was therefore determined according to the present CH-peaks and subtracted from the total H_2O -related broadband (Figure A1c). The half-height of the CH-bands in the region of 2,860–2,960 cm^{-1} , as well as the H_2O overestimation in the region of 3,000–3,800 cm^{-1} , were calculated for each quartz spectrum separately.

A3. Treatment of Quartzite IR Spectra

After subtracting the H_2O overestimation related to the epoxy, the quartz spectra were deconvoluted into a sum of Gaussian curves. This separated molecular H_2O from discrete OH peaks (Figure A1d). Two broad Gaussian curves corresponding to the symmetric and asymmetric stretching bands of molecular H_2O (located at 3,280 and 3,490 cm^{-1} , respectively) were used to simulate the broad band of H_2O absorption centered around 3,400 cm^{-1} . According to Kats (1962), Aines and Rossman (1984), Aines et al. (1984), Kronenberg et al. (1986), Niimi et al. (1999), Stünitz et al. (2017), and Jollands et al. (2020), the Gaussian curves used to simulate discrete OH peaks are positioned at following wave numbers (cm^{-1}):

- 3,699—part of phyllosilicate peak triplet;
- 3,653—part of phyllosilicate peak triplet;
- 3,624—part of phyllosilicate peak triplet;
- 3,596— H^+ compensating for charge near Al^{3+} substituting for Si^{4+} ;
- 3,585— OH^- structurally bound in dislocation cores;
- 3,467—?
- 3,429—part of Al-triplet;
- 3,379—part of Al-triplet;
- 3,319—part of Al-triplet.

Appendix B: Digitized Maps of LCD and HCD Domains

Recrystallization was quantified from digitized (polygonized) LCD and HCD domains for increasing content of H_2O (Figure B1), showing the proportions of recrystallized material in the most deformed parts of the weaker samples.

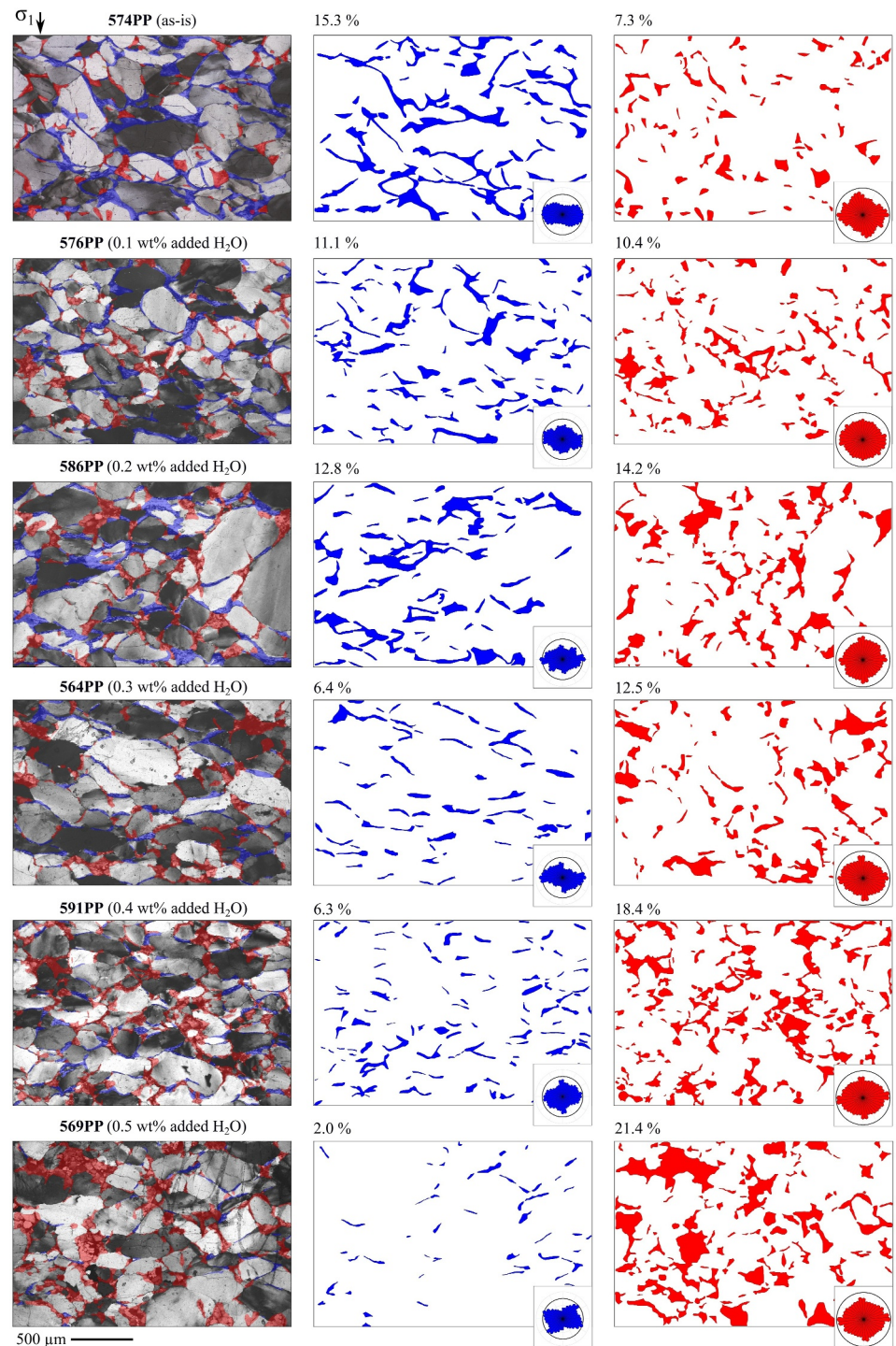


Figure B1. Digitized maps of low crack density (blue) and high crack density (red) recrystallized domains superposed on the cross polarized micrographs of the most deformed areas of the samples, covering H₂O-addition range from 0 to 0.5 wt.%. The area fraction is indicated above each map. Rose diagrams in the bottom right corners show orientation distribution of segmented domain boundaries with respect to the shortening direction, with the black circle marking proportion of 3%.

Appendix C: Major Elements in the Quenched Melt

List of major constituents of the quenched melt from amorphous pockets with their average concentrations in samples within the investigated H₂O-addition range. The average concentrations are calculated as arithmetic mean of 10 measurements for each sample and expressed in wt.%.

H ₂ O-addition	SiO ₂	Al ₂ O ₃	H ₂ O	Na ₂ O	K ₂ O	MgO	CaO	FeO	TiO ₂
0	69.94	11.67	11.01	0.35	4.84	0.21	0.21	0.95	0.20
0.1	68.08	11.84	11.90	0.46	5.46	0.24	0.20	1.10	0.22
0.2	69.94	10.62	12.19	0.35	5.11	0.22	0.15	0.86	0.27
0.3	71.36	11.40	11.44	1.62	3.39	0.13	0.01	0.00	0.23
0.4	70.28	11.84	11.20	1.48	4.03	0.11	0.07	0.21	0.24
0.5	69.11	12.90	12.27	2.22	2.60	0.12	0.06	0.00	0.07

The amorphous phase preserved in the samples was imaged and analyzed with the scanning electron microscope Tescan VEGA equipped with the energy-dispersive spectroscope X-Max 50 (Oxford Instruments) (SEM-EDS) at the Institute of Petrology and Structural Geology, Charles University in Prague. This method was preferred over the use of the electron probe microanalyzer (EPMA) due to the possibility of considerably lower probe current, which is more suitable for the analysis of an amorphous silicate phase rich in H₂O and alkali elements. The analyses were performed with accelerating voltage 15 kV and probe current 1.5 nA. Instead of spot mode with focussed beam, a square area of size 3 × 3 μm was scanned during each acquisition in order to minimize damage of the analyzed glass. The spectra were acquired for 50 s of live time, and following standards were used for the quantification of the analyzed elements: Na—albite; Mg—periclase; Al—topaz; Si—diopside; P—apatite; Cl—tugtupite; K—sanidine; Ca—diopside; Ti—rutile; Fe—almandine. K-series of the characteristic X-rays were used for detection of all elements. The XPP method (Pouchou & Pichoir, 1985) was used for the correction of matrix effects.

Appendix D: Distribution of Other Elements With Respect to the H₂O-Addition

The melt pockets, although rarely found in high-H₂O samples, show some systematic differences in chemistry of the quenched melt. Comparing low- and high-H₂O samples, and according to the relative differences in content of K₂O and Na₂O, we can observe decrease in K-feldspar and increase in albite components in the melt, while the content of silica remains stable. On the other hand, increase in Na₂O with addition of H₂O could result from a higher influx of Na from an external source (i.e., salt pieces used as a confining medium), which is potentially indicative also from increase of Cl. However, this increase in Na₂O appears to reflect a decrease not only in K₂O and FeO (Figure D1a), but also in Mg, P, and Ca (Figure D1b). Results of Grundy, Liu, et al. (2008) and Grundy, Jung, et al. (2008) have shown that higher concentrations of Na₂O with respect to K₂O, CaO, and MgO in the SiO₂- and Al₂O₃-stable systems at ~1,000 C° decrease viscosity of the silicate melt. The higher Na/K, Na/Ca, and Na/Mg ratios in our high-H₂O samples (Figure D1c) thus might cause the melt to be more fluid and easier to migrate.

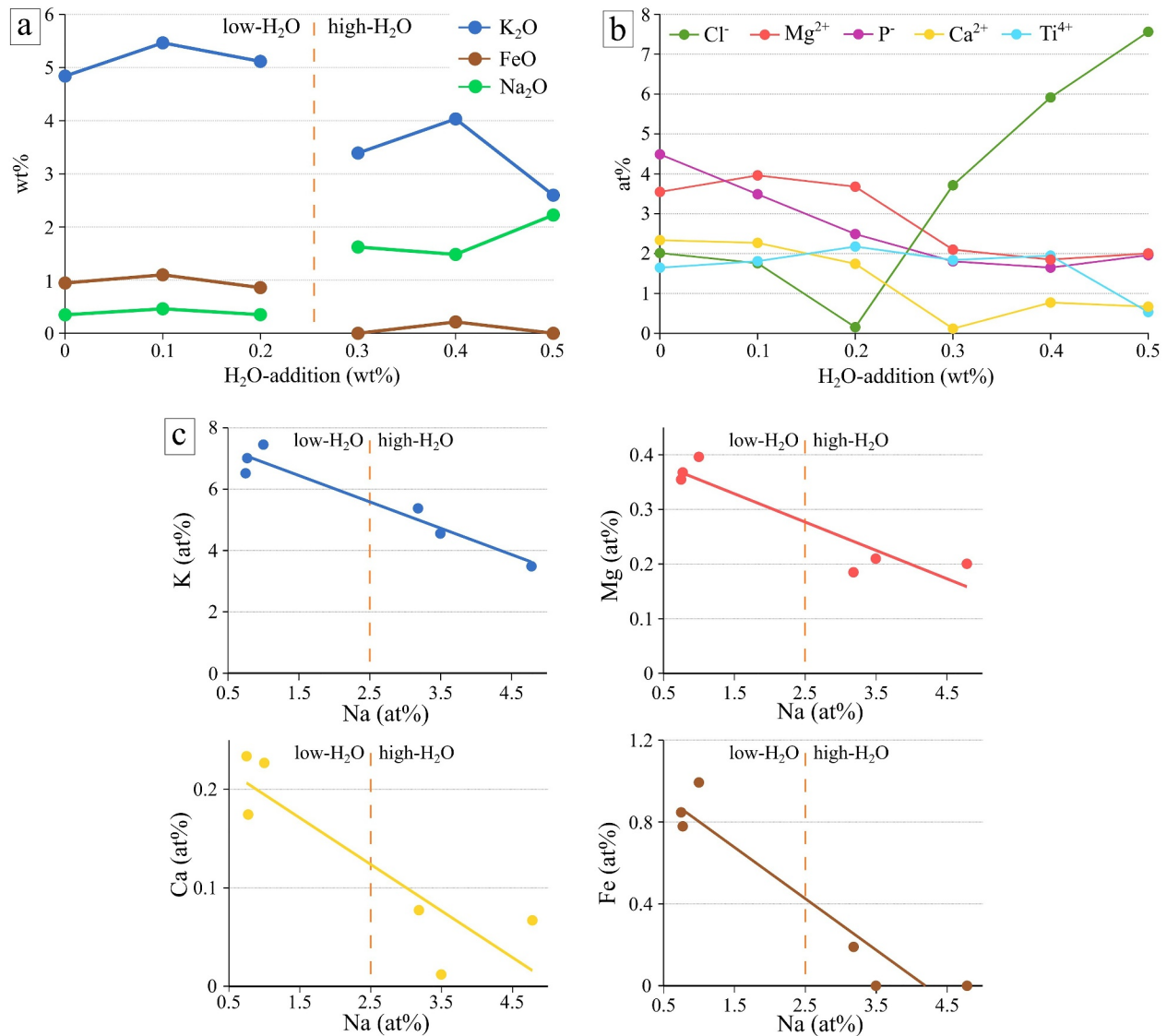


Figure D1. Average (arithmetic mean) values of (a) K₂O, FeO, and Na₂O contents shown in wt.%, and (b) Cl⁻, Mg²⁺, P⁻, Ca²⁺, and Ti⁴⁺ contents shown in atomic percent (at%), in samples with 0–0.5 wt.% of added H₂O. (c) Changes in content of K, Ca, Mg, and Fe with respect to content of Na, shown in at%.

Appendix E: List of the FTIR-Subjected Samples

List of samples and details of FTIR measurements. Mean thick section thicknesses are presented with one sigma standard deviation. Number of measurements is separated for the least deformed grains (LD), the most deformed grains (MD) and GB.

Sample	H ₂ O addition (wt.%)	Mean thick section thickness (μm)	Number of measurements		
			LD	MD	GB
568PP	0	124.6 ± 4.9	52	83	69
574PP	0	116.1 ± 11.3	68	81	75
567PP	0.1	100.1 ± 6.6	62	83	64
576PP	0.1	126.2 ± 5.9	73	115	81
566PP	0.2	102.3 ± 10.5	43	85	56
586PP	0.2	129.3 ± 6.7	92	145	89
564PP	0.3	114.8 ± 11.5	70	75	78
588PP	0.3	97.3 ± 8.5	92	115	77
591PP	0.4	115.3 ± 8.3	71	77	76
569PP	0.5	101.3 ± 10.5	53	90	64
597PP	0.5	122.8 ± 13.6	86	95	85

Appendix F: Distribution of OH-Discrete Peaks

Discrete Al- and mica-related OH-bands show the highest average absorbance at the grain boundary regions, while their lowest concentrations were obtained from interiors of the most deformed grains (Figure F1).

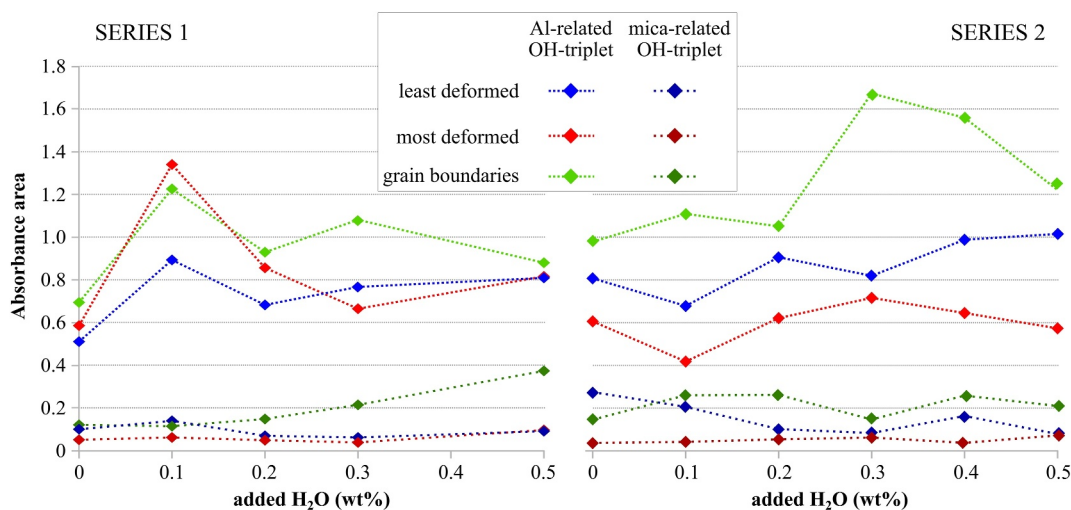


Figure F1. Amounts and distribution of OH-related discrete peaks to Al and phyllosilicates in deformed samples of two experimental series. Results plotted as dots (Al-related OH-peak triplet) and diamonds (mica-related OH-peaks triplet) present average values of all successful measurements for each sample and measuring category. The dashed and dotted lines represent the average values (arithmetic mean) of all measurements for particular H₂O-addition. Values for the least deformed grains are presented in shades of blue, values for the most deformed grains in red, and values for the grain boundaries in green. Lighter shades correspond to concentrations of OH⁻ related to Al, while darker shades correspond to OH⁻ related to mica.

Appendix G: Non-Thermionic Cathodoluminescence of Deformation Regions

The cold CL images allow a thorough strain analysis using the original sand grains, and estimate on the relative amount of quenched melt channels (bright clusters and trails in Figure G1). The quenched melt from these areas was separated by color thresholding and superposed on the manually redrawn original sand grains in Figure 13.

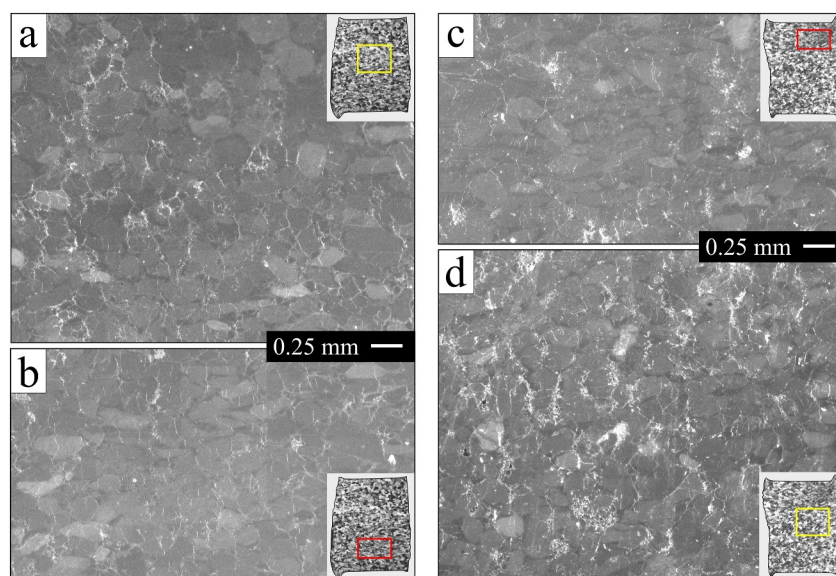


Figure G1. Non-thermionic cathodoluminescence micrographs of the strain-analyzed regions marked by rectangles in Figure 12, showing the distribution and density of the pockets and cracks filled with amorphous matter, visible as bright trails and clusters. The images in (a) and (b) show the areas with lower, and in (b) and (c), with higher particle strain, in (a, b) the weaker sample 591PP and (c, d) the stronger sample 565PP. Images were transformed to grayscale for better visibility of the melt-related features.

Data Availability Statement

The experimental and analytical data files used in this paper are available through the Mendeley Digital Repository at: <https://doi.org/10.17632/c5x5whjx42.1> (Pongrac, 2023). This data provides (a) Original files from the deformation experiments with all the data were recorded with frequency of 1 s, (b) Original FTIR spectra from two experimental sets with H₂O addition range 0–0.5 wt.% (for H₂O amount in samples, check Table 1 in the article) and (c) Most important original EBSD files (.ctf). Recorded parameters in the mechanical data are time (ti) stress (fi), confining pressure (pci) and displacement of sigma-1 (deformation) piston (dxi). The stress-strain curves from the mechanical data were constructed using RIG version 1.3. (Pec, 2010) available at <http://mpec.scripts.mit.edu/peclab/software/>. All the EBSD-related data were developed with MTEX version 5.1.1. (Bachmann et al., 2010) available at <https://mte-toolbox.github.io/index> and PolyLX version 1.3. (Lexa, 2003a) available at <https://petrol.natur.cuni.cz/~ondro/oldweb/polylx/home>. The quantitative microstructural analysis and the strain analysis of digitized original grains was performed by the Python polyLX package (Lexa, 2023) available at <https://github.com/ondrolexa/polylx> (Bachmann et al., 2010; Lexa, 2003a, 2003b; Pec, 2010; Pongrac, 2023).

References

- Aines, R. D., Kirby, S. H., & Rossman, G. R. (1984). Hydrogen speciation in synthetic quartz. *Physics and Chemistry of Minerals*, 11(5), 204–212. <https://doi.org/10.1007/BF00308135>
- Aines, R. D., & Rossman, G. R. (1984). Water in minerals? A peak in the infrared. *Journal of Geophysical Research*, 89(B6), 4059–4071. <https://doi.org/10.1029/jb089ib06p04059>
- Bachmann, F., Hielscher, R., & Schaeben, H. (2010). Texture analysis with MTEX—free and open source software toolbox. Version 5.1.1 [Software]. *GitHub*. Retrieved from <https://mte-toolbox.github.io/index>
- Bachmann, F., Hielscher, R., & Schaeben, H. (2011). Grain detection from 2D and 3D EBSD data—Specification of the MTEX algorithm. *Ultramicroscopy*, 111(12), 1720–1733. <https://doi.org/10.1016/j.ultramic.2011.08.002>

Acknowledgments

We would like to acknowledge financial support from the Grant agency of Charles University (GAUK 488119) and the Center of Geosphere Dynamics (UNCE/SCI/006). We thank Rune Stien and Raoul Heilbronner for the assistance during the material sampling within the ELKEM quarry in the Austertana region. A. Slodczyk is thanked for the assistance and helpful suggestions regarding FTIR measurements, R. Jedlička for assistance in acquiring the CL and EMPA maps, and P. Zavada for the help during cold CL microscopy. The critical reviews by Michael Stipp and an anonymous reviewer have helped to improve the manuscript substantially. Open access publishing facilitated by Univerzita Karlova, as part of the Wiley - CzechELib agreement.

- Beeler, N. M., Hirth, G., Thomas, A., & Bürgmann, R. (2016). Effective stress, friction, and deep crustal faulting. *Journal of Geophysical Research: Solid Earth*, *121*(2), 1040–1059. <https://doi.org/10.1002/2015JB012115>
- Blacic, J. D. (1975). Plastic-deformation mechanisms in quartz: The effect of water. *Tectonophysics*, *27*(3), 271–294. [https://doi.org/10.1016/0040-1951\(75\)90021-9](https://doi.org/10.1016/0040-1951(75)90021-9)
- Brace, W. F., & Martin, R. J. (1968). A test of the law of effective stress for crystalline rocks of low porosity. *International Journal of Rock Mechanics and Mining Sciences*, *5*(5), 415–426. [https://doi.org/10.1016/0148-9062\(68\)90045-4](https://doi.org/10.1016/0148-9062(68)90045-4)
- Brace, W. F., Walsh, J. B., & Frangos, W. T. (1968). Permeability of granite under high pressure. *Journal of Geophysical Research*, *73*(6), 2225–2236. <https://doi.org/10.1029/jb073i006p02225>
- Bureau, H., & Keppler, H. (1999). Complete miscibility between silicate melts and hydrous fluids in the upper mantle: Experimental evidence and geochemical implications. *Earth and Planetary Science Letters*, *165*(2), 187–196. [https://doi.org/10.1016/S0012-821X\(98\)00266-0](https://doi.org/10.1016/S0012-821X(98)00266-0)
- Chopra, P. N., & Paterson, M. S. (1984). The role of water in the deformation of dunite. *Journal of Geophysical Research*, *89*(B9), 7861–7876. <https://doi.org/10.1029/JB089iB09p07861>
- Cionoiu, S., Moulas, E., Stünitz, H., & Tajčmanová, L. (2022). Locally resolved stress-state in samples during experimental deformation: Insights into the effect of stress on mineral reactions. *Journal of Geophysical Research: Solid Earth*, *127*(8), e2022JB024814. <https://doi.org/10.1029/2022JB024814>
- Den Brok, S. W. J. (1998). Effect of microcracking on pressure-solution strain rate: The Gratz grain-boundary model. *Geology*, *26*(10), 915–918. [https://doi.org/10.1130/0091-7613\(1998\)026<0915:eomops>2.3.co;2](https://doi.org/10.1130/0091-7613(1998)026<0915:eomops>2.3.co;2)
- Dieterich, J. H., & Kilgore, B. D. (1996). Imaging surface contacts: Power law contact distributions and contact stresses in quartz, calcite, glass and acrylic plastic. *Tectonophysics*, *256*(1–4), 219–239. [https://doi.org/10.1016/0040-1951\(95\)00165-4](https://doi.org/10.1016/0040-1951(95)00165-4)
- Doukhan, J. C. (1995). Lattice defects and mechanical behaviour of quartz SiO₂. *Journal de Physique III*, *5*(11), 1809–1832. <https://doi.org/10.1051/jp3:1995228>
- Farver, J. R., & Yund, R. A. (1992). Oxygen diffusion in a fine-grained quartz aggregate with wetted and nonwetted microstructures. *Journal of Geophysical Research*, *97*(B10), 14017–14029. <https://doi.org/10.1029/92jb01206>
- Finch, M. A., Weinberg, R. F., & Hunter, N. J. R. (2016). Water loss and the origin of thick ultramylonites. *Geology*, *44*(8), 599–602. <https://doi.org/10.1130/G37972.1>
- Fischer, G. J., & Paterson, M. S. (1989). Dilatancy during rock deformation at high temperatures and pressures. *Journal of Geophysical Research*, *94*(B12), 17607–17617. <https://doi.org/10.1029/jb094i12p17607>
- Fitz Gerald, J. D., Boland, J. N., McLaren, A. C., Ord, A., & Hobbs, B. E. (1991). Microstructures in water-weakened single crystals of quartz. *Journal of Geophysical Research*, *96*(B2), 2139–2155. <https://doi.org/10.1029/90jb02190>
- French, M., Hirth, G., & Okazaki, K. (2019). Fracture-induced pore fluid pressure weakening and dehydration of serpentinite. *Tectonophysics*, *767*, 228168. <https://doi.org/10.1016/j.tecto.2019.228168>
- Gerretsen, J., Paterson, M. S., & McLaren, A. C. (1989). The uptake and solubility of water in quartz at elevated pressure and temperature. *Physics and Chemistry of Minerals*, *16*(4), 334–342. <https://doi.org/10.1007/BF00199553>
- Ghosh, S., Stünitz, H., Raimbourg, H., & Précigout, J. (2022). Quartz rheology constrained from constant-load experiments: Consequences for the strength of the continental crust. *Earth and Planetary Science Letters*, *597*, 117814. <https://doi.org/10.1016/j.epsl.2022.117814>
- Gleason, G. C., & DeSisto, S. (2008). A natural example of crystal-plastic deformation enhancing the incorporation of water into quartz. *Tectonophysics*, *446*(1–4), 16–30. <https://doi.org/10.1016/j.tecto.2007.09.006>
- Griggs, D. (1967). Hydrolytic weakening of quartz and other silicates. *Geophysical Journal of the Royal Astronomical Society*, *14*(1–4), 19–31. <https://doi.org/10.1111/j.1365-246X.1967.tb06218.x>
- Griggs, D. (1974). A model of hydrolytic weakening in quartz. *Journal of Geophysical Research*, *79*(11), 1653–1661. <https://doi.org/10.1029/jb079i011p01653>
- Grundy, A. N., Jung, I. H., Pelton, A. D., & Decterov, S. A. (2008b). A model to calculate the viscosity of silicate melts Part II: The NaO 0.5-MgO-CaO-AlO_{1.5}-SiO₂ system. *International Journal of Materials Research*, *99*(11), 1195–1209. <https://doi.org/10.3139/146.101753>
- Grundy, A. N., Liu, H., Jung, I. H., Decterov, S. A., & Pelton, A. D. (2008a). A model to calculate the viscosity of silicate melts Part I: Viscosity of binary SiO₂-MeOx systems (Me = Na, K, Ca, Mg, Al). *International Journal of Materials Research*, *99*(11), 1185–1194. <https://doi.org/10.3139/146.101752>
- Handin, J., Hager, R. V., Friedman, M., & Feathers, J. N. (1963). Experimental deformation of sedimentary rocks under confining pressure: Pore pressure tests. *AAPG Bulletin*, *47*, 716–755. <https://doi.org/10.1306/bc743a87-16be-11d7-8645000102c1865d>
- Heilbronner, R., & Barrett, S. (2014). Image analysis in earth sciences: Microstructures and textures of earth materials. In *Image analysis in Earth Sciences: Microstructures and textures of Earth materials*. Springer. <https://doi.org/10.1007/978-3-642-10343-8>
- Hielscher, R., & Schaeben, H. (2008). A novel pole figure inversion method: Specification of the MTEX algorithm. *Journal of Applied Crystallography*, *41*(6), 1024–1037. <https://doi.org/10.1107/S0021889808030112>
- Hirth, G., & Beeler, N. M. (2015). The role of fluid pressure on frictional behavior at the base of the seismogenic zone. *Geology*, *43*(3), 223–226. <https://doi.org/10.1130/G36361.1>
- Hirth, G., & Tullis, J. (1992). Dislocation creep regimes in quartz aggregates. *Journal of Structural Geology*, *14*(2), 145–159. [https://doi.org/10.1016/0191-8141\(92\)90053-Y](https://doi.org/10.1016/0191-8141(92)90053-Y)
- Holyoke, C. W., & Kronenberg, A. K. (2010). Accurate differential stress measurement using the molten salt cell and solid salt assemblies in the Griggs apparatus with applications to strength, piezometers and rheology. *Tectonophysics*, *494*(1–2), 17–31. <https://doi.org/10.1016/j.tecto.2010.08.001>
- Ito, Y., & Nakashima, S. (2002). Water distribution in low-grade siliceous metamorphic rocks by micro-FTIR and its relation to grain size: A case from the Kanto mountain region, Japan. *Chemical Geology*, *189*(1–2), 1–18. [https://doi.org/10.1016/S0009-2541\(02\)00022-0](https://doi.org/10.1016/S0009-2541(02)00022-0)
- Jaoul, O., Tullis, J., & Kronenberg, A. (1984). Effect of varying water contents on the creep behavior of Heavtreet quartzite. *Journal of Geophysical Research*, *89*(B6), 4298–4312. <https://doi.org/10.1029/jb089i06p04298>
- Jollands, M. C., Blanchard, M., & Balan, E. (2020). Structure and theoretical infrared spectra of OH defects in quartz. *European Journal of Mineralogy*, *32*(3), 311–323. <https://doi.org/10.5194/ejm-32-311-2020>
- Kats, A. (1962). Hydrogen in alpha-quartz. In *Philips Research Reports* (Vol. 17).
- Kilian, R., Heilbronner, R., Holyoke, C. W., Kronenberg, A. K., & Stünitz, H. (2016). Dislocation creep of dry quartz. *Journal of Geophysical Research: Solid Earth*, *121*(5), 3278–3299. <https://doi.org/10.1002/2015JB012771>
- King Hubbert, M., & Rubey, W. W. (1959). Role of fluid pressure in mechanics of overthrust faulting: I. Mechanics of fluid-filled porous solids and its application to overthrust faulting. *Bulletin of the Geological Society of America*, *70*(2), 115. [https://doi.org/10.1130/0016-7606\(1959\)70\[115:ROFPIM\]2.0.CO;2](https://doi.org/10.1130/0016-7606(1959)70[115:ROFPIM]2.0.CO;2)

- Kohlstedt, D. L., Bai, Q., Wang, Z. C., & Mei, S. (2000). Rheology of partially molten rocks. In *Physics and chemistry of partially molten rocks* (pp. 3–28).
- Kohlstedt, D. L., Evans, B., & Mackwell, S. J. (1995). Strength of the lithosphere: Constraints imposed by laboratory experiments. *Journal of Geophysical Research*, *100*(B9), 17587–17602. <https://doi.org/10.1029/95jb01460>
- Kronenberg, A. K. (1994). Hydrogen speciation and chemical weakening of quartz. *Silica*, *29*, 123–176.
- Kronenberg, A. K., Ashley, K. T., Francis, M. K., Holyoke, C. W., Jezek, L., Kronenberg, J. A., et al. (2020). Water loss during dynamic recrystallization of Moine thrust quartzites, northwest Scotland. *Geology*, *48*(6), 557–561. <https://doi.org/10.1130/G47041.1>
- Kronenberg, A. K., Hasnan, H. F. B., Holyoke, C. W., Law, R. D., Liu, Z., & Thomas, J. B. (2017). Synchrotron FTIR imaging of OH in quartz mylonites. *Solid Earth*, *8*(5), 1025–1045. <https://doi.org/10.5194/se-8-1025-2017>
- Kronenberg, A. K., Kirby, S. H., Aines, R. D., & Rossman, G. R. (1986). Solubility and diffusional uptake of hydrogen in quartz at high water pressures: Implications for hydrolytic weakening. *Journal of Geophysical Research*, *91*(B12), 12723–12741. <https://doi.org/10.1029/jb091ib12p12723>
- Kronenberg, A. K., Segall, P., & Wolf, G. H. (1990). Hydrolytic weakening and penetrative deformation within a natural shear zone. *AGU Geophysical Monograph*, *56*, 21–36. <https://doi.org/10.1029/gm056p0021>
- Kronenberg, A. K., & Tullis, J. (1984). Flow strengths of quartz aggregates: Grain size and pressure effects due to hydrolytic weakening. *Journal of Geophysical Research*, *89*(B6), 4281–4297. <https://doi.org/10.1029/jb089ib06p04281>
- Kronenberg, A. K., & Wolf, G. H. (1990). Fourier transform infrared spectroscopy determinations of intragranular water content in quartz-bearing rocks: Implications for hydrolytic weakening in the laboratory and within the earth. *Tectonophysics*, *172*(3–4), 255–271. [https://doi.org/10.1016/0040-1951\(90\)90034-6](https://doi.org/10.1016/0040-1951(90)90034-6)
- Lexa, O. (2003a). Numerical approach in structural and microstructural analyses.
- Lexa, O. (2003b). PolyLX toolbox for MATLAB™ [Software]. *Version 1.3*. Retrieved from <https://petrol.natur.cuni.cz/~ondro/oldweb/polylx/home>
- Lexa, O. (2023). PolyLX—Python package to visualize and analyze digitized 2D microstructures [Software]. *GitHub*. Retrieved from <https://github.com/ondrolexa/polylx>
- Libowitzky, E., & Rossman, G. R. (1997). An IR absorption calibration for water in minerals. *American Mineralogist*, *82*(11–12), 1111–1115. <https://doi.org/10.2138/am-1997-11-1208>
- Luan, F. C., & Paterson, M. S. (1992). Preparation and deformation of synthetic aggregates of quartz. *Journal of Geophysical Research*, *97*(B1), 301–320. <https://doi.org/10.1029/91jb01748>
- Mackwell, S. J., Kohlstedt, D. L., & Paterson, M. S. (1985). The role of water in the deformation of olivine single crystals. *Journal of Geophysical Research*, *90*(B13), 11319–11333. <https://doi.org/10.1029/jb090ib13p11319>
- Manning, C. E. (2004). The chemistry of subduction-zone fluids. *Earth and Planetary Science Letters*, *223*(1–2), 1–16. <https://doi.org/10.1016/j.epsl.2004.04.030>
- McLaren, A. C., Fitz Gerald, J. D., & Gerretsen, J. (1989). Dislocation nucleation and multiplication in synthetic quartz: Relevance to water weakening. *Physics and Chemistry of Minerals*, *16*(5), 465–482. <https://doi.org/10.1007/BF00197016>
- Menegon, L., Nasipuri, P., Stünitz, H., Behrens, H., & Ragna, E. (2011). Dry and strong quartz during deformation of the lower crust in the presence of melt. *Journal of Geophysical Research*, *116*(10), B10410. <https://doi.org/10.1029/2011JB008371>
- Morrison-Smith, D. J., Paterson, M. S., & Hobbs, B. E. (1976). An electron microscope study of plastic deformation in single crystals of synthetic quartz. *Tectonophysics*, *33*(1–2), 43–79. [https://doi.org/10.1016/0040-1951\(76\)90051-2](https://doi.org/10.1016/0040-1951(76)90051-2)
- Morrow, C., Radney, B., & Byerlee, J. (1992). Frictional strength and the effective pressure law of Montmorillonite and Illite Clays. *International Geophysics*, *51*(C), 69–88. [https://doi.org/10.1016/S0074-6142\(08\)62815-6](https://doi.org/10.1016/S0074-6142(08)62815-6)
- Nakashima, S., Matayoshi, H., Yuko, T., Michibayashi, K., Masuda, T., Kuroki, N., et al. (1995). Infrared microspectroscopy analysis of water distribution in deformed and metamorphosed rocks. *Tectonophysics*, *245*(3–4), 263–276. [https://doi.org/10.1016/0040-1951\(94\)00239-6](https://doi.org/10.1016/0040-1951(94)00239-6)
- Nègre, L., Stünitz, H., Raimbourg, H., Lee, A., Précigout, J., Pongrac, P., & Jéřábek, P. (2021). Effect of pressure on the deformation of quartz aggregates in the presence of H₂O. *Journal of Structural Geology*, *148*, 104351. <https://doi.org/10.1016/j.jsg.2021.104351>
- Ni, H., Zhang, L., Xiong, X., Mao, Z., & Wang, J. (2017). Supercritical fluids at subduction zones: Evidence, formation condition, and physicochemical properties. In *Earth-science reviews* (Vol. 167, pp. 62–71). Elsevier B.V. <https://doi.org/10.1016/j.earscirev.2017.02.006>
- Niimi, N., Aikawa, N., & Shinoda, K. (1999). The infrared absorption band at 3596 cm⁻¹ of the recrystallized quartz from Mt. Takamiyama, southwest Japan. *Mineralogical Magazine*, *63*(5), 693–701. <https://doi.org/10.1180/minmag.1999.063.5.07>
- Olgaard, D. L., Ko, S. C., & Wong, T. F. (1995). Deformation and pore pressure in dehydrating gypsum under transiently drained conditions. *Tectonophysics*, *245*(3–4), 237–248. [https://doi.org/10.1016/0040-1951\(94\)00237-4](https://doi.org/10.1016/0040-1951(94)00237-4)
- Palazzin, G., Raimbourg, H., Stünitz, H., Heilbronner, R., Neufeld, K., & Précigout, J. (2018). Evolution in H₂O contents during deformation of polycrystalline quartz: An experimental study. *Journal of Structural Geology*, *114*, 95–110. <https://doi.org/10.1016/j.jsg.2018.05.021>
- Panozzo, R. H. (1983). Two-dimensional analysis of shape-fabric using projections of digitized lines in a plane. *Tectonophysics*, *95*(3–4), 279–294. [https://doi.org/10.1016/0040-1951\(83\)90073-2](https://doi.org/10.1016/0040-1951(83)90073-2)
- Paterson, M. (1982). The determination of hydroxyl by infrared absorption in quartz, silicate glasses and similar materials. *Bulletin de Mineralogie*, *105*(1), 20–29. <https://doi.org/10.3406/bulmi.1982.7582>
- Paterson, M. S. (1989). The interaction of water with quartz and its influence in dislocation flow: An overview. In *Rheology of solids and of the Earth* (pp. 107–142).
- Pec, M. (2010). RIG: A MATLAB program for evaluation of mechanical data from experimental apparatuses [Software]. *Version 1.3*. Retrieved from <http://mpec.scripts.mit.edu/peclab/software/>
- Pec, M. (2014). Experimental investigation on the rheology of fault rocks.
- Pec, M., Stünitz, H., Heilbronner, R., & Drury, M. (2016). Semi-brittle flow of granitoid fault rocks in experiments. *Journal of Geophysical Research: Solid Earth*, *121*(3), 1677–1705. <https://doi.org/10.1002/2015JB012513>
- Pevik, J. A. (2015). Geological and mineralogical characterization of the upper part of the Gamasfjell quartzite at the Vaggecearu mountain.
- Pirzer, M., & Sawatzki, J. (2006). Method and Device for correcting a spectrum. In *US Patents*.
- Pongrac, P. (2023). Experimental data [Dataset]. *Mendeley Data*, *V1*. <https://doi.org/10.17632/c5x5whjx42.1>
- Pongrac, P., Jéřábek, P., Stünitz, H., Raimbourg, H., Heilbronner, R., Racek, M., & Nègre, L. (2022). Mechanical properties and recrystallization of quartz in presence of H₂O: Combination of cracking, subgrain rotation and dissolution-precipitation processes. *Journal of Structural Geology*, *160*, 104630. <https://doi.org/10.1016/J.JSG.2022.104630>
- Post, A., & Tullis, J. (1998). The rate of water penetration in experimentally deformed quartzite: Implications for hydrolytic weakening. *Tectonophysics*, *295*(1–2), 117–137. [https://doi.org/10.1016/S0040-1951\(98\)00145-0](https://doi.org/10.1016/S0040-1951(98)00145-0)

- Pouchou, J. L., & Pichoir, F. (1985). PAP ([phi][rho] z) procedure for improved quantitative microanalysis. In J. T. Armstrong (Ed.), *Microbeam analysis* (pp. 104–106). Press.
- Renner, J., Evans, B., & Hirth, G. (2000). On the rheologically critical melt fraction. *Earth and Planetary Science Letters*, *181*(4), 585–594. [https://doi.org/10.1016/S0012-821X\(00\)00222-3](https://doi.org/10.1016/S0012-821X(00)00222-3)
- Rosenberg, C. L., & Handy, M. R. (2005). Experimental deformation of partially melted granite revisited: Implications for the continental crust. *Journal of Metamorphic Geology*, *23*(1), 19–28. <https://doi.org/10.1111/j.1525-1314.2005.00555.x>
- Rovetta, M. R., Holloway, J. R., & Blacic, J. D. (1986). Solubility of hydroxyl in natural quartz annealed in water at 900°C and 1.5 GPa. *Geophysical Research Letters*, *13*(2), 145–148. <https://doi.org/10.1029/GL013i002p00145>
- Rutter, E. H., & Brodie, K. H. (2004). Experimental intracrystalline plastic flow in hot-pressed synthetic quartzite prepared from Brazilian quartz crystals. *Journal of Structural Geology*, *26*(2), 259–270. [https://doi.org/10.1016/s0191-8141\(03\)00096-8](https://doi.org/10.1016/s0191-8141(03)00096-8)
- Schmocker, M., Bystricky, M., Kunze, K., Burlini, L., Stünitz, H., & Burg, J.-P. (2003). Granular flow and Riedel band formation in water-rich quartz aggregates experimentally deformed in torsion. *Journal of Geophysical Research*, *108*(B5), 2242. <https://doi.org/10.1029/2002jb001958>
- Scholz, C. H., & Cowie, P. A. (1990). Determination of total strain from faulting using slip measurements. *Nature*, *346*(6287), 837–839. <https://doi.org/10.1038/346837a0>
- Seaman, S. J., Williams, M. L., Jercinovic, M. J., Koteas, G. C., & Brown, L. B. (2013). Water in nominally anhydrous minerals: Implications for partial melting and strain localization in the lower crust. *Geology*, *41*(10), 1051–1054. <https://doi.org/10.1130/G34435.1>
- Stalder, R. (2021). OH point defects in quartz—a review. *European Journal of Mineralogy*, *33*(2), 145–163. <https://doi.org/10.5194/ejm-33-145-2021>
- Stipp, M., Tullis, J., & Behrens, H. (2006). Effect of water on the dislocation creep microstructure and flow stress of quartz and implications for the recrystallized grain size piezometer. *Journal of Geophysical Research*, *111*(4), B04201. <https://doi.org/10.1029/2005JB003852>
- Stünitz, H., Raimbourg, H., Nègre, L., Précigout, J., Jollands, M., Pongrac, P., et al. (2024). Evolution of H₂O content in deforming quartz aggregates: An experimental study. *Journal of Structural Geology*, *178*, 105029. <https://doi.org/10.1016/j.jsg.2023.105029>
- Stünitz, H., Thust, A., Heilbronner, R., Behrens, H., Kilian, R., Tarantola, A., & Fitz Gerald, J. D. (2017). Water redistribution in experimentally deformed natural milky quartz single crystals—Implications for H₂O-weakening processes. *Journal of Geophysical Research: Solid Earth*, *122*(2), 866–894. <https://doi.org/10.1002/2016JB013533>
- Tarantola, A., Diamond, L. W., & Stünitz, H. (2010). Modification of fluid inclusions in quartz by deviatoric stress I: Experimentally induced changes in inclusion shapes and microstructures. *Contributions to Mineralogy and Petrology*, *160*(6), 825–843. <https://doi.org/10.1007/s00410-010-0509-z>
- Tarantola, A., Diamond, L. W., Stünitz, H., Thust, A., & Pec, M. (2012). Modification of fluid inclusions in quartz by deviatoric stress. III: Influence of principal stresses on inclusion density and orientation. *Contributions to Mineralogy and Petrology*, *164*(3), 537–550. <https://doi.org/10.1007/s00410-012-0749-1>
- Terzaghi, K. (1943). Theoretical Soil mechanics. In *Theoretical Soil Mechanics*. <https://doi.org/10.1002/9780470172766>
- Thomas, A. M., Bürgmann, R., Shelly, D. R., Beeler, N. M., & Rudolph, M. L. (2012). Tidal triggering of low frequency earthquakes near Parkfield, California: Implications for fault mechanics within the brittle-ductile transition. *Journal of Geophysical Research*, *117*(B5), B05301. <https://doi.org/10.1029/2011jb009036>
- Thomas, S. M., Koch-Müller, M., Reichart, P., Rhede, D., Thomas, R., Wirth, R., & Matsyuk, S. (2009). IR calibrations for water determination in olivine, r-GeO₂, and SiO₂ polymorphs. *Physics and Chemistry of Minerals*, *36*(9), 489–509. <https://doi.org/10.1007/s00269-009-0295-1>
- Tullis, J., & Yund, R. A. (1980). Hydrolytic weakening of experimentally deformed Westerly granite and Hale albite rock. *Journal of Structural Geology*, *2*(4), 439–451. [https://doi.org/10.1016/0191-8141\(80\)90005-X](https://doi.org/10.1016/0191-8141(80)90005-X)
- Tullis, J., & Yund, R. A. (1989). Hydrolytic weakening of quartz aggregates: The effects of water and pressure on recovery. *Geophysical Research Letters*, *16*(11), 1343–1346. <https://doi.org/10.1029/GL016i011p01343>
- Tullis, T. E., & Tullis, J. (1986). Experimental rock deformation techniques. In *Mineral and rock deformation: Laboratory studies* (36th ed., pp. 297–324). American Geophysical Union. <https://doi.org/10.1029/gm036p0297>
- Vollbrecht, A., Stipp, M., & Olesen, N. Ø. (1999). Crystallographic orientation of microcracks in quartz and inferred deformation processes: A study on gneisses from the German continental deep Drilling Project (KTB). *Tectonophysics*, *303*(1–4), 279–297. [https://doi.org/10.1016/s0040-1951\(98\)00265-0](https://doi.org/10.1016/s0040-1951(98)00265-0)